# How Strain and Spin may make a Star Bi-Polar

Lawrence K. Forbes
School of Mathematics and Physics
University of Tasmania
Private Bag 37, Hobart, Tasmania, AUSTRALIA. *

August 2013, revised November 2013, January 2014.

**Abstract**

A previous study by Forbes (2011b) has argued that, when a light fluid is injected from a point source into a heavier ambient fluid, the interface between them is most unstable to perturbations at the lowest spherical mode. This means that, regardless of initial conditions, the outflow from a point source eventually becomes a one-sided jet. However, two-sided (bi-polar) outflows are nevertheless often observed in astrophysics, in apparent contradiction to this prediction. While there are many possible explanations for this fact, the present paper considers the effect of a straining flow in the ambient fluid. In addition, solid-body rotation in the inner fluid is also accounted for, in a Boussinesq viscous model. It is shown analytically that there are circumstances under which straining flow alone is sufficient to convert the one-sided jet into a genuine bi-polar outflow, in linearized theory. This is confirmed in a numerical solution of a viscous model of the flow, based on a spectral solution technique that accounts for nonlinear effects. Rotation can also generate flows that are two sided, and this is likewise revealed through an asymptotic analysis and numerical solutions of the non-linear equations.

**Keywords:** bi-polar flows, Boussinesq approximation, instability, interface, one-sided outflows, Rayleigh-Taylor flow, rotation, spectral methods, straining flow, vorticity.

*mailto:Larry.Forbes@utas.edu.au

# 1 Introduction

In the classical Rayleigh-Taylor instability, two fluids of different density form two horizontal layers, with an interface separating them and the more dense fluid on top. This configuration is unstable, so that small disturbances to the interface grow with time and develop into fingers of one fluid penetrating into the other. The problem was first investigated by Rayleigh (1883) and Taylor (1950) in the context of linearized theory, in which disturbances to the interface are assumed to be of small amplitude. They found that disturbances grow exponentially fast, so that eventually their amplitude must become large enough to violate the assumptions of linear theory. Consequently, non-linearity becomes important after some finite time.

This work assumed that the two fluids are inviscid, and while this gives rise to Laplace's equation for the velocity potential in each fluid, which is a relatively simple linear partial differential equation, the conditions on the unknown evolving interface nevertheless remain non-linear. That fact is responsible for some surprisingly intricate behaviour at the interface. It was observed in earlier numerical solutions of the problem that the calculations failed after a certain time, as discussed by Sharp (1984), for reasons that were not immediately obvious. It is now known from the work of Moore (1979), on the related Kelvin-Helmholtz instability, that a curvature singularity forms at the interface within finite time. Beyond that critical time, the inviscid model ceases to be valid. A similar process occurs for the Rayleigh-Taylor instability, and Moore's analysis has since been used by Baker, Caflisch and Siegel (1993) to estimate the time at which a curvature singularity forms at the interface in this situation. For the Kelvin-Helmholtz instability, Moore's (1979) observation that a curvature singularity is formed at finite time has been confirmed by Cowley, Baker and Tanveer (1999), using an asymptotic argument in which time is treated as a complex variable.

The inclusion of viscosity in models of the Rayleigh-Taylor instability eliminates the curvature singularity at the interface. Instead, a small region of high vorticity is produced, at the precise time and location where the inviscid theory predicted a singularity. This was shown numerically by Forbes (2009), in planar Rayleigh-Taylor flow, but has been understood to be the case for a long time. Krasny (1986) simulated the effects of viscosity in an otherwise inviscid fluid by introducing a "vortex blob" approach, in which the interface is effectively modelled as a diffuse region rather than a mathematical discontinuity. For the Kelvin-Helmholtz instability, his calculations could continue to much later times than that at which Moore's (1979) curvature singularity would occur. He demonstrated that the interface rolled up into overhanging plumes at later times. Baker and Pham (2006) have argued that

different types of "vortex blob" methods may result in different outcomes for these unstable flows, so that the results are not entirely independent of the details of the numerical method. Nevertheless, these techniques are capable of generating solutions in broad agreement with the results of numerical solutions of fully viscous equations, as has been illustrated by Tryggvason et al. (1991).

The Rayleigh-Taylor instability has been studied extensively, and it arises in a number of situations of practical interest, including in the atmosphere (see Schmitt (1995)) and ocean (see Cui and Street (2004)). It is also believed to play a significant role in astrophysics, as discussed in the review by Inogamov (1999). McClure-Griffiths et al. (2003) attributed the structures they observed in radio studies of galaxies to Rayleigh-Taylor flows, and they may also play a role in galactic super-bubble formation, as suggested by Low and McCray (1988). Dgani and Soker (1998) undertook careful observations of 34 planetary nebulae, and suggested that the Rayleigh-Taylor instability might explain the fragmentation of the halo of nebulae, so that the interstellar medium could penetrate to their inner regions.

Rayleigh-Taylor type instabilities are possible in geometries more elaborate than the relatively simple situation of two horizontal layers in two-dimensional flow, that represents the classical statement of the problem. In particular, it is possible to conceive of these types of flows in astrophysical circumstances, provided that there is a radially inwardly directed gravity force, with a "heavier" fluid enclosing a bubble of "lighter" fluid. In this present paper, such a flow is of interest purely as a type of canonical problem in fundamental fluid mechanics; however, it does also have more than a little relevance to problems in astrophysics, concerning the shapes adopted by planetary nebulae with outflows (see Huarte-Espinosa et al. (2012)) or a type of re-bound phenomenon that may occur after an initial implosion in a neutron star, as discussed by Nordhaus et al. (2012). Of course, magnetic fields are almost certainly of importance in such applications, and a discussion of their role in flows around young stars is given by Shariff (2009). They are not considered here, although further modelling of their effect on radial outflow from a line source is given by Chambers and Forbes (2012).

Forbes (2011a) has recently considered a generalization of the classical Rayleigh-Taylor flow to a geometry in which a lighter fluid is injected into a heavier medium, through a line source. The flow is therefore still two-dimensional, as in the classical problem, but now gravity is directed radially inwards. Small perturbations to the interface were found to grow unstably as the outflow progressed. In the inviscid formulation of the problem, curvature singularities were encountered at the interface within finite time, analogously to those predicted by Moore (1979) for the planar Kelvin-Helmholtz insta-

bility. When viscous effects were then included, the curvature singularities were again replaced by small regions of high vorticity, and these resulted in the formation of overturning plumes arranged around the expanding cylinder. Qualitatively similar results have been generated by Matsuoka and Nishihara (2006) for a related shock-induced flow (the Richtmyer-Meshkov instability).

For cylindrical planar flows of this type, as well as for more complex three-dimensional geometries, the curvature of the interface can result in an additional instability, known as the Bell-Plesset effect. This has been analyzed by Mikaelian (2005) in linearized (small amplitude) theory, for concentric shells of fluid undergoing implosion or explosion, in both cylindrical and spherical geometry. Forbes (2011b) studied outflow from a point source, with an initially spherical interface and inwardly directed gravity. For inviscid fluids, he presented a linearized analysis and showed that it reduces to Mikaelian's equation at infinite Froude number (zero gravity), corresponding to an underwater explosion, for example. Interestingly, this small-amplitude solution predicts that the first spherical mode is the most unstable, so that any initial disturbance would ultimately be dominated by it as time progresses. Thus it would be expected that the outflow would develop into a one-sided jet. Non-linear inviscid theory could not confirm this decisively, since again it was found that a type of curvature singularity developed at the interface; nevertheless, Forbes (2011b) also carried out the numerical solution to a viscous model and demonstrated numerically that one-sided outflows were indeed produced.

In the astrophysical context, this represents something of a paradox, since it is commonly observed that outflows occur as strongly two-sided (bi-polar) jets, and this is discussed in the book by Stahler and Palla (2004, section 13.2.1) and the review by Zinnecker and Yorke (2007). Of course, magnetic field effects might account for this in part, with the star acting as a strong magnetic dipole. However, the numerical work of Lovelace et al. (2010), in which magnetic fields are included, does nevertheless produce one-sided outflow jets, and they have been observed experimentally in astrophysics, as is discussed by Reipurth and Bally (2001). One-sided jets are also observed in certain spherical implosions in the internal confinement fusion literature, and are described further by Ye et al. (2010).

One purpose of the present paper is to explore the extent to which the one-sided jet produced from spherical outflow, as a result of the Bell-Plesset effect, is affected by motion of the ambient heavier fluid. In the astrophysical context, this would correspond to background motion of the interstellar medium. This is now known to be an important phenomenon; Low and Klessen (2004) and Inoue and Fukui (2013) argue that supersonic turbulence and cloud-cloud collision are likely to have important roles in star forma-

tion, and this is confirmed both theoretically and in observations. Klein and Woods (1998) carried out a numerical study of two colliding clouds, and noted that perturbations on the cloud surfaces may indeed lead to asymmetrical outflows, through a "bending mode instability". Observations of head-on collisions in galaxies have been presented by Braine et al. (2004). The computations of Anathpindika (2009) show two clouds of similar size colliding and forming an elongated straining-type region, and it is suggested that star formation may occur in this zone.

In the present paper, the focus is on fundamental fluid mechanics, and so a simple straining flow is considered in the outer fluid, perhaps as an idealization of the flow computed by Anathpindika (2009), for example. A very simple model of this effect has been given recently by Forbes and Brideson (2013) and assumes that the densities of the inner and outer fluids are approximately equal; in that case, the problem reduces to a non-linear partial differential equation for the shape of the interface alone, since the velocities in each fluid are able to be specified in advance. Those authors showed that their non-linear equation can be solved completely in closed form, and gives a perfectly symmetric bi-polar outflow as a result of the straining motion superposed on the outflow from the point source. A question of interest is therefore to know under what conditions the one-sided jet produced when the densities are no longer equal might be forced into a bi-polar configuration by the background straining flow. A secondary aim of this paper is to allow for solid-body rotation of the inner jacket of fluid surrounding the point source, so that its effects on the outflow morphology can be assessed.

Section 2 presents the governing equations for the non-linear inviscid model for this problem. As with the analysis of Forbes (2011b), it has been found here that curvature singularities are formed at the interface at relatively early times, and these prevent features of any particular interest from being seen in the results. Thus, although these non-linear inviscid equations have been solved using a spectral method, the results are not discussed here. However, the linearized analysis is nevertheless still of interest, and it shows how there are situations in which the straining flow can indeed render the outflow bi-polar. When rotation is included in the inner fluid, a linearized theory is no longer available; however, a new approximate theory is presented in Section 3, and likewise demonstrates that rotation may also result in bi-polar outflow. A Boussinesq approach to the full viscous problem is then presented in section 4. Straining is included, and provision is also made for solid-body rotation of the inner fluid. The results of these computations are presented in section 5 and some concluding remarks given in section 6.

## 2 Linearized Inviscid Analysis

A spherical bubble of radius $a$ is supposed to be present at the initial time $t = 0$, with its centre located at the origin of a cartesian coordinate system. It is filled with incompressible fluid of density $\rho_1$ , and at time $t = 0$ a mass source at the origin is impulsively turned on. This source produces fluid at the volume rate $m$. The bubble is embedded in an outer ambient fluid of density $\rho_2$ . A straining flow is present in the outer fluid, and is characterized by straining rate parameter $A$, with units time$^{-1}$. In general it will be assumed that the outer fluid 2 has larger density than inner fluid 1, so that their ratio obeys the condition $D = \rho_2/\rho_1 > 1$. The object at the origin, which is responsible for the mass outflow, is modelled as a mathematical point source, but it also has mass $\mathcal{M}$ and so generates a gravitational potential $G\mathcal{M}/\sqrt{x^2+y^2+z^2}$ per mass, in which $G$ is the universal gravitational constant. In the inviscid model, a sharp interface is present between the fluids, and it will be assumed here that the geometry remains axi-symmetric, for simplicity.

It is appropriate to express this problem in terms of spherical polar coordinates, as defined in the text by Kreyszig (2011). The distance from the origin is $r = \sqrt{x^2+y^2+z^2}$, the azimuthal angle about the $z$-axis is $\theta$ , and $\phi$ is the angle of declination measured down from the $z$-axis. Since the problem is assumed axi-symmetric, solutions will be independent of angle $\theta$. It follows that

$$\begin{aligned} x &= r\sin\phi\cos\theta \qquad & 0 < r < \infty \\ y &= r\sin\phi\sin\theta \qquad & 0 < \phi < \pi \\ z &= r\cos\phi \qquad & 0 < \theta < 2\pi. \end{aligned} \tag{2.1}$$

The interface in this inviscid problem is assumed to have the equation $r = R(\phi, t)$ so that $R(\phi, 0) = a$ at the initial time $t = 0$.

Dimensionless variables are now introduced, and these are used throughout the paper. The initial radius $a$ is taken as the unit of length, and time is referenced against the quantity $a^3/m$. Speeds are made dimensionless by reference to $m/a^2$ and the ratio $\rho_1 m^2/a^4$ is used as the scale for pressure. For inviscid fluids, the velocity vector $\mathbf{q}$ may be derived as the gradient of a velocity potential $\Phi$ which is non-dimensionalized by reference to $m/a$. The three key dimensionless parameters are therefore

$$D = \frac{\rho_2}{\rho_1} \quad ; \quad F^2 = \frac{m^2}{G\mathcal{M}a^3} \tag{2.2}$$

and a non-dimensional strain rate parameter $A$ for the outer fluid. The

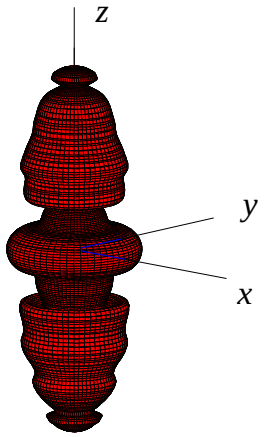


Figure 1: A sketch of the dimensionless outflow configuration for a rotating inner fluid in the presence of a straining flow. This image is taken from an actual solution for viscous flow at time $t = 4$, with $A = 0.1$, density ratio $D = 1.05$, Froude number $F = 0.5$, angular speed $\omega = 0.2$ and the $n = 2$ mode perturbed with initial amplitude $\epsilon = 0.1$. The "interface" has been constructed from the $\bar{\rho} = 0.01$ contour for the density perturbation function.

quantity $D$ is the ratio of densities, and $F$ is a Froude number. A sketch of a dimensionless outflow is given in Figure 1.

In the spherical coordinates (2.1), the velocity vector is expressed as $\mathbf{q} = u\mathbf{e_r} + w\mathbf{e}_\phi$ with components $u$ and $w$ in the radial and axial directions, respectively. In each fluid, these components are obtained from their velocity potentials according to the relationships

$$u_j = \frac{\partial \Phi_j}{\partial r} \qquad w_j = \frac{1}{r}\frac{\partial \Phi_j}{\partial \phi}, \tag{2.3}$$

for $j = 1, 2$. Since the fluids are also incompressible, each velocity potential satisfies Laplace's equation

$$\nabla^2 \Phi_j = \frac{\partial^2 \Phi_j}{\partial r^2} + \frac{2}{r}\frac{\partial \Phi_j}{\partial r} + \frac{1}{r^2}\frac{\partial^2 \Phi_j}{\partial \phi^2} + \frac{\cot\phi}{r^2}\frac{\partial \Phi_j}{\partial \phi} = 0. \tag{2.4}$$

There is a point source located at the origin and also an imposed straining flow, so that the velocity potential

$$\Phi = -\frac{1}{4\pi r} + Ar^2 P_2(\cos\phi) \tag{2.5}$$

serves as a background flow for each fluid. In this expression, which itself is a solution to Laplace's equation (2.4), the function $P_2(z) = (1/2)(3z^2 - 1)$ represents the Legendre polynomial of order 2, as defined in Abramowitz and Stegun (1972, page 333).

The interface $r = R(\phi, t)$ starts as a sphere of radius 1 at time $t = 0$, but then evolves according to the two kinematic conditions

$$u_j = \frac{\partial R}{\partial t} + \frac{w_j}{R}\frac{\partial R}{\partial \phi} \quad j = 1, 2 \quad \text{on } r = R(\phi, t) \tag{2.6}$$

and the dynamic condition

$$\begin{aligned} & D\frac{\partial \Phi_2}{\partial t} - \frac{\partial \Phi_1}{\partial t} + \tfrac{1}{2}D\left(u_2^2 + w_2^2\right) - \tfrac{1}{2}\left(u_1^2 + w_1^2\right) - \frac{(D-1)}{F^2 r} \\ = \; & \tfrac{1}{2}\frac{(D-1)}{\left(4\pi R_0^2\right)^2} - \frac{(D-1)}{F^2 R_0} \qquad \text{on } r = R(\phi, t). \end{aligned} \tag{2.7}$$

The kinematic expressions (2.6) represent the fact that neither of the two fluids is free to cross the interface. The pressures in each fluid may be obtained from the unsteady Bernoulli equation, as given by Batchelor (1967, page 383), and the dynamic condition (2.7) is then a statement that the two

pressures must be equal at the interface. In this expression, the reference radius function

$$R_0(t) = \left[1 + \frac{3t}{4\pi}\right]^{1/3} \tag{2.8}$$

is the shape that the interface $r = R(\phi, t)$ would adopt in the absence of any straining flow and if it remained purely spherical. A derivation of the expression (2.7) is given in Forbes (2011b).

In this Section, the initial conditions will be taken to be that the interface itself is spherical, but that a perturbation of magnitude $\epsilon$ is made to the speed, at the $n$-th spherical harmonic. Consequently,

$$\begin{aligned} \Phi_1(r, \phi, 0) &= -\frac{1}{4\pi r} + Ar^2 P_2(\cos\phi) + \frac{\epsilon}{n} r^n P_n(\cos\phi) \\ \Phi_2(r, \phi, 0) &= -\frac{1}{4\pi r} + Ar^2 P_2(\cos\phi) - \frac{\epsilon}{n+1} r^{-n-1} P_n(\cos\phi). \end{aligned} \tag{2.9}$$

In these expressions, the functions $P_n(z)$ are Legendre polynomials of order $n$, as for the pure straining background flow (2.5).

Numerical solutions to these non-linear equations have been generated using a spectral technique similar to that in Forbes (2011b), but the results are insufficiently interesting to merit inclusion here. This is because curvature singularities are formed at the poles within quite short time intervals, and this process is only enhanced by the presence of the straining field, as the strain rate $A$ is increased. The inclusion of viscous effects is far more revealing, and this is considered in Section 4. Instead, a linearized solution to these equations is developed here, based on the assumption that the perturbation to the spherical interface, and hence also the straining field, are both proportional to the small parameter $\epsilon$ in the initial conditions (2.9).

The two velocity potentials are expanded in series in the small parameter $\epsilon$, and take the forms

$$\begin{aligned} \Phi_1(r, \phi, t) &= -\frac{1}{4\pi r} + \epsilon A_1 r^2 P_2(\cos\phi) + \epsilon \Phi_{11}(r, \phi, t) + \mathcal{O}\left(\epsilon^2\right) \\ \Phi_2(r, \phi, t) &= -\frac{1}{4\pi r} + \epsilon A_1 r^2 P_2(\cos\phi) + \epsilon \Phi_{21}(r, \phi, t) + \mathcal{O}\left(\epsilon^2\right). \end{aligned} \tag{2.10}$$

Notice that the strain rate parameter $A$ is also assumed small, so that $A = \epsilon A_1$. The velocity components can now be obtained from equations (2.3). Similarly, the shape of the interface is perturbed about the basic spherical form, and is given by the expression

$$R(\phi, t) = R_0(t) + \epsilon R_1(\phi, t) + \mathcal{O}\left(\epsilon^2\right), \tag{2.11}$$

in which the zeroth-order term $R_0$ is the spherical radius function given in equation (2.8). These expressions (2.10), (2.11) are substituted into the governing equations, and terms are retained only to the first order in $\epsilon$, giving a system of linearized equations for the three unknown functions $\Phi_{11}$ , $\Phi_{21}$ and $R_1$ . The two kinematic conditions (2.6) yield

$$\begin{aligned}
\frac{\partial R_1}{\partial t} &= -\frac{2R_1}{4\pi R_0^3} + 2A_1 R_0 P_2(\cos\phi) + \frac{\partial \Phi_{11}}{\partial r} \\
\frac{\partial R_1}{\partial t} &= -\frac{2R_1}{4\pi R_0^3} + 2A_1 R_0 P_2(\cos\phi) + \frac{\partial \Phi_{21}}{\partial r} \\
&\qquad \text{on } r = R_0(t)
\end{aligned} \tag{2.12}$$

and the dynamic condition (2.7) can be expressed in the form

$$\begin{aligned}
D\frac{\partial \Phi_{21}}{\partial t} - \frac{\partial \Phi_{11}}{\partial t} + \frac{(D-1)}{4\pi R_0^2}\frac{\partial R_1}{\partial t} + \frac{(D-1)}{F^2}\frac{R_1}{R_0^2} = 0 \\
\text{on } r = R_0(t),
\end{aligned} \tag{2.13}$$

where use has been made of equations (2.12).

Since the velocity potentials must satisfy Laplace's equation (2.4) in their respective domains, it follows that the two linearized components in (2.10) have the general forms

$$\begin{aligned}
\Phi_{11}(r,\phi,t) &= \sum_{n=1}^{\infty} B_{n1}(t) r^n P_n(\cos\phi), \quad 0 < r < R_0(t) \\
\Phi_{21}(r,\phi,t) &= \sum_{n=1}^{\infty} C_{n1}(t) r^{-n-1} P_n(\cos\phi), \quad r > R_0(t).
\end{aligned} \tag{2.14}$$

Similarly, the perturbed radius function in equation (2.11) is written

$$R_1(\phi,t) = \sum_{n=1}^{\infty} R_{n1}(t) P_n(\cos\phi). \tag{2.15}$$

These are now substituted into equations (2.12), (2.13) to give differential equations for the unknown coefficients $B_{n1}(t)$, $C_{n1}(t)$ and $R_{n1}(t)$.

In the linearized solution, each of the Fourier modes in the series (2.14), (2.15) acts independently of the others, so that each mode can be considered separately. After some algebra, it may be shown that the coefficients for the perturbed interface function (2.15) obey the second-order linear (non-

constant coefficient) differential equation

$$\frac{d^2R_{n1}}{dt^2}R_0(Dn+n+1)+\frac{dR_{n1}}{dt}\left[\frac{3(Dn+n+1)}{4\pi R_0^2}\right]$$
$$-R_{n1}\left[\frac{2[(n+2)(n+1)-Dn(n-1)]}{(4\pi)^2R_0^5}+\frac{(D-1)n(n+1)}{F^2R_0^2}\right]=0$$
$$\text{if } n\neq 2, \tag{2.16}$$

except at the second Fourier-Legendre mode, when the equation becomes

$$\frac{d^2R_{21}}{dt^2}R_0(2D+3)+\frac{dR_{21}}{dt}\frac{3(2D+3)}{4\pi R_0^2}$$
$$-R_{21}\left[\frac{4(6-D)}{(4\pi)^2R_0^5}+\frac{6(D-1)}{F^2R_0^2}\right]=A_1\frac{20D}{4\pi R_0}$$
$$\text{if } n=2. \tag{2.17}$$

These equations (2.16), (2.17) for the coefficients $R_{n1}$ of the linearized solution (2.15) determine the shape of the outflow, in small amplitude theory. The question of most interest here is whether the bi-polar mode is ultimately dominant, as a result of the straining motion with amplitude $A_1$. If this is the case, then the function $R_{21}$ in equation (2.17) will grow faster than all the other modes $R_{n1}$ , $n \neq 2$, as $t \to \infty$. If, however, one-sided jets are ultimately formed, then $R_{11}$ will become the dominant coefficient, regardless of the straining amplitude $A_1$. The linearized equation (2.16) for $n \neq 2$ was apparently first derived by Plesset (1954) in the limiting case $F = \infty$, and is also presented for that case by Mikaelian (2005) (his equation 1c).

It is relevant to the present investigation to consider the behaviour of solutions to equations (2.16), (2.17) in various parameter regimes, to determine whether one-sided or bi-polar outflows may result. Forbes (2011b) claimed that a closed-form solution to (2.16) would not be possible for arbitrary values of the parameters; however, such a solution does in fact exist, and can be represented in terms of modified Bessel functions. For completeness this new solution is given in Appendix A (Section 8) , but nevertheless does not lend itself to easy analysis. For finite Froude number $F$ and arbitrary density ratio $D$, it appears that the first-mode function $R_{11}$ obtained from equation (2.16) grows faster than the bi-polar mode $R_{21}$ in equation (2.17), so that one-sided outflows are most commonly predicted by this linearized analysis, for arbitrary straining amplitude $A_1$. Of course, it has been assumed here that the straining rate $A = \epsilon A_1$ is also small, and larger values are certainly possible, that do not conform to the assumptions of this linearized theory. In such cases, numerical solution of a non-linear problem is required, and will

be studied in Section 5. There is, however, an interesting limiting case of this general linearized result, and this is now considered separately here.

## 2.1 Infinite Froude number limit

It is of interest here to study separately the infinite Froude-number case $F = \infty$. This is not directly accounted for in the general closed-form solution presented in Appendix A (Section 8), since one of the changes of variable needed there assumed finite Froude number.

Infinite Froude number corresponds to the limit in which the mass of the source is small, so that the effects of gravity are insignificant. As in Appendix A (Sec. 8), the spherical radius $R_0$ in equation (2.8) is taken to be the independent variable, instead of the time $t$. In the infinite Froude-number limit, equation (2.16) then becomes

$$R_0^2 \frac{d^2 R_{n1}}{dR_0^2} + R_0 \frac{dR_{n1}}{dR_0} - \alpha_n^2 R_{n1} = 0, \quad \text{if } n \neq 2$$
$$\text{with } \alpha_n^2 = 2\left[\frac{(n+2)(n+1) - Dn(n-1)}{Dn + n + 1}\right], \tag{2.18}$$

and at the second mode, equation (2.17) yields

$$R_0^2 \frac{d^2 R_{21}}{dR_0^2} + R_0 \frac{dR_{21}}{dR_0} - \alpha_2^2 R_{21} = A_1 \beta_2 R_0^4, \quad \text{if } n = 2$$
$$\text{with } \alpha_2^2 = \frac{4(6-D)}{(2D+3)}, \quad \beta_2 = \frac{80\pi D}{(2D+3)}. \tag{2.19}$$

Each of these equations is of Euler-Cauchy type, and can be solved in closed form.

When $n \neq 2$, equation (2.18) is easily seen to have general solution

$$R_{n1}(R_0) = C_{n1} R_0^{\alpha_n} + C_{n2} R_0^{-\alpha_n} \tag{2.20}$$

for arbitrary constants $C_{n1}$ and $C_{n2}$. On the other hand, the inhomogeneous equation (2.19), in which the second mode is forced by the straining flow, has solution

$$R_{21}(R_0) = C_{21} R_0^{\alpha_2} + C_{22} R_0^{-\alpha_2} + A_1 \frac{\beta_2 (2D+3)}{12(3D+2)} R_0^4. \tag{2.21}$$

Again, the constants $C_{21}$ and $C_{22}$ are arbitrary.

The solution (2.20) shows that disturbances to the interface do not grow if $\alpha_n$ is purely imaginary. Consequently, the $n$-th spherical Fourier mode is stable if

$$D > \frac{(n+2)(n+1)}{n(n-1)}, \tag{2.22}$$

and this is the result obtained by Forbes (2011b). If equation (2.22) is not obeyed, then the interface will be unstable and grow algebraically with time, for infinite Froude number. In particular, the first mode $n = 1$ is always unstable regardless of the value of the density ratio $D$. Furthermore, instability always occurs for $D < 1$, unlike pure Rayleigh-Taylor flow, and this indicates the additional destabilizing effect of the spherical geometry, known as the Bell-Plesset effect, as discussed by Epstein (2004). In the case of the second mode $n = 2$, it is clear from equation (2.21) that the solution grows at the rate $R_0^4$ as a result of the straining flow. This is always greater than the growth rate of the unstable first mode $n = 1$, which grows only at the power $\sqrt{12/(D+2)}$. Therefore, at infinite Froude number $F$, the first mode is always unstable and any initial disturbance will develop into a one-sided jet, when there is no straining. However, any non-zero straining amplitude $\epsilon A_1$ eventually causes the second mode to dominate, so that a bi-polar jet is ultimately formed.

In summary this Section has shown that, in the linearized solution, the inclusion of a straining flow with small strain rate is unlikely to prevent the ultimate formation of a one-sided jet. However, when gravity effects are negligible, so that $F = \infty$, then straining does indeed convert the one-sided jet into a bi-polar outflow.

# 3 Asymptotic Inviscid Theory with Rotation

Rotation of the inner bubble of fluid 1 is also of interest in this study. However, this situation does not lend itself to a linearized analysis in the same way as for straining flow in section 2, since the fluid pressures are *quadratic* in the azimuthal velocity component $v$ responsible for the rotation. Nevertheless, it is possible to derive a weakly non-linear asymptotic theory similar to that in section 2. This is presented here.

The analysis starts from Euler's equations of motion for incompressible fluids, expressed in spherical polar coordinates. In each fluid, the velocity components $(u, w, v)$ in the $(r, \phi, \theta)$ directions and the pressures are expressed

by means of the expansions

$$\begin{aligned} u_j &= \frac{1}{4\pi r^2} + \epsilon\tilde{U}_j + \mathcal{O}\left(\epsilon^2\right) \\ w_j &= \epsilon\tilde{W}_j + \mathcal{O}\left(\epsilon^2\right) \\ v_1 &= \sqrt{\epsilon}\tilde{V}_1 + \mathcal{O}\left(\epsilon^{3/2}\right) \\ p_j &= p_j^0(r,t) + \epsilon\tilde{P}_j + \mathcal{O}\left(\epsilon^2\right), \qquad j = 1,2, \\ R &= R_0(t) + \epsilon\tilde{R}_1 + \mathcal{O}\left(\epsilon^2\right), \end{aligned} \tag{3.1}$$

in which $\epsilon$ is again a small parameter. The two functions $p_1^0$ and $p_2^0$ are the background pressures in each fluid, required to satisfy Euler's equations in the presence of the point source, subject to the conditions that pressure be continuous on the expanding spherical interface $r = R_0(t)$ in equation (2.8) and zero at infinity. These two functions are therefore

$$\begin{aligned} p_1^0(r,t) &= \frac{1}{rF^2} - \frac{1}{2}\frac{1}{(4\pi)^2 r^4} + \frac{(D-1)}{R_0F^2} - \frac{1}{2}\frac{(D-1)}{(4\pi)^2 R_0^4}, \quad 0 < r < R_0(t) \\ p_2^0(r,t) &= \frac{D}{rF^2} - \frac{1}{2}\frac{D}{(4\pi)^2 r^4}, \quad r > R_0(t). \end{aligned} \tag{3.2}$$

These expressions (3.1), (3.2) are substituted into the full inviscid Euler equations. Terms are retained to order $\epsilon$ in the radial and axial components of the momentum equations, and to order $\sqrt{\epsilon}$ in the azimuthal component. In each fluid, the continuity equations yield

$$\frac{1}{r^2}\frac{\partial}{\partial r}\left(r^2\tilde{U}_j\right) + \frac{1}{r\sin\phi}\frac{\partial}{\partial\phi}\left(\tilde{W}_j\sin\phi\right) = 0, \qquad j = 1,2. \tag{3.3}$$

The three components of the (Euler) momentum equation in inner fluid 1 then give

$$\begin{aligned} \frac{\partial\tilde{U}_1}{\partial t} + \frac{1}{4\pi r^2}\frac{\partial\tilde{U}_1}{\partial r} - \frac{2}{4\pi r^3}\tilde{U}_1 - \frac{\tilde{V}_1^2}{r} + \frac{\partial\tilde{P}_1}{\partial r} &= 0 \\ \frac{\partial\tilde{W}_1}{\partial t} + \frac{1}{4\pi r^2}\frac{\partial\tilde{W}_1}{\partial r} + \frac{1}{4\pi r^3}\tilde{W}_1 - \frac{\cot\phi}{r}\tilde{V}_1^2 + \frac{1}{r}\frac{\partial\tilde{P}_1}{\partial\phi} &= 0 \\ \frac{\partial\tilde{V}_1}{\partial t} + \frac{1}{4\pi r^2}\frac{\partial\tilde{V}_1}{\partial r} + \frac{1}{4\pi r^3}\tilde{V}_1 &= 0. \end{aligned} \tag{3.4}$$

These equations hold in the domain $0 < r < R_0(t)$, in which the function $R_0$ is as given in equation (2.8). There is no rotation in outer fluid 2, and so the azimuthal momentum equation in that case is satisfied identically. The

radial and axial components become

$$\begin{aligned}\frac{\partial \tilde{U}_2}{\partial t}+\frac{1}{4\pi r^2}\frac{\partial \tilde{U}_2}{\partial r}-\frac{2}{4\pi r^3}\tilde{U}_2+\frac{1}{D}\frac{\partial \tilde{P}_2}{\partial r} &= 0\\ \frac{\partial \tilde{W}_2}{\partial t}+\frac{1}{4\pi r^2}\frac{\partial \tilde{W}_2}{\partial r}+\frac{1}{4\pi r^3}\tilde{W}_2+\frac{1}{Dr}\frac{\partial \tilde{P}_2}{\partial \phi} &= 0,\end{aligned} \tag{3.5}$$

and these are valid over the domain $r > R_0(t)$. The two kinematic conditions (2.6) yield

$$\frac{\partial \tilde{R}_1}{\partial t}=\tilde{U}_j-\frac{2}{4\pi R_0^3}\tilde{R}_1 \qquad j=1,2 \quad \text{on } r=R_0(t). \tag{3.6}$$

The dynamic condition, that the two pressures must be equal on the interface, gives rise to the approximate constraint

$$\tilde{P}_2-\tilde{P}_1=\big(D-1\big)\left[\frac{1}{R_0^2F^2}-\frac{2}{(4\pi)^2R_0^5}\right]\tilde{R}_1 \quad \text{on } r=R_0(t). \tag{3.7}$$

This is a consistent weakly non-linear model of inviscid outflow, with rotation in the inner fluid region. It must be solved subject to the initial condition

$$\tilde{V}_1(r,\phi,0)=\omega_0 r\sin\phi, \qquad 0<r<R_0(0) \tag{3.8}$$

on the azimuthal component of the fluid velocity vector.

To maintain complete consistency in this weakly non-linear model, the last equation for $\tilde{V}_1$ in the system (3.4) should be solved subject to the initial condition (3.8) and then utilized in the remaining components of the momentum equation (3.4). While this is in principle achievable, it is sufficiently difficult as to make useful progress impossible. Therefore, in order to proceed, the asymptotic approximation is now made that the initial azimuthal velocity in equation (3.8) may be taken to be the solution for all times $t$ of practical interest. This form is now used in the radial and axial momentum components of Euler's equation (3.4).

Following a similar procedure to that in Section 2, the velocity components in inner fluid 1 are expressed by means of the series

$$\begin{aligned}\tilde{U}_1(r,\phi,t) &= \sum_{n=1}^{\infty} nB_{n1}(t)r^{n-1}P_n\left(\cos\phi\right)\\ \tilde{W}_1(r,\phi,t) &= -\sum_{n=1}^{\infty} B_{n1}(t)r^{n-1}P_n'\left(\cos\phi\right)\sin\phi, \quad 0<r<R_0(t).\end{aligned} \tag{3.9}$$

In outer fluid 2, the velocity components are likewise written

$$\begin{aligned}\tilde{U}_2(r,\phi,t) &= -\sum_{n=1}^{\infty}(n+1)C_{n1}(t)r^{-n-2}P_n(\cos\phi)\\ \tilde{W}_2(r,\phi,t) &= -\sum_{n=1}^{\infty}C_{n1}(t)r^{-n-2}P_n'(\cos\phi)\sin\phi, \quad r>R_0(t). \quad (3.10)\end{aligned}$$

The shape of the interface is determined by the function $\tilde{R}_1$ and it is represented by the same form (2.15) as used previously in Section 2. These are substituted into equations (3.4), (3.5) and the boundary conditions (3.6) and (3.7) to give differential equations for the coefficients $B_{n1}(t)$, $C_{n1}(t)$ and $R_{n1}(t)$.

To satisfy the weakly non-linear approximation (3.4) to Euler's equation in the inner fluid, with azimuthal velocity component given by (3.8), it is necessary that the perturbation pressure in that region take the form

$$\begin{aligned}\tilde{P}_1(r,\phi,t) &= \frac{1}{2}\omega_0^2 r^2\sin^2\phi - \sum_{n=1}^{\infty}B_{n1}'(t)r^nP_n(\cos\phi)\\ &- \frac{1}{4\pi}\sum_{n=1}^{\infty}nB_{n1}(t)r^{n-3}P_n(\cos\phi)+f_1(t), \quad 0<r<R_0(t). \quad (3.11)\end{aligned}$$

in which $f_1(t)$ is so far an arbitrary function of time. Similarly, Euler's equation (3.5) requires that the pressure in the outer fluid be given by the expression

$$\begin{aligned}\tilde{P}_2(r,\phi,t) &= -D\sum_{n=1}^{\infty}C_{n1}'(t)r^{-n-1}P_n(\cos\phi)\\ &+ \frac{D}{4\pi}\sum_{n=1}^{\infty}(n+1)C_{n1}(t)r^{-n-4}P_n(\cos\phi), \quad r>R_0(t). \quad (3.12)\end{aligned}$$

The perturbation pressure in equation (3.12) is required to fall to zero as $r\to\infty$.

As in the previous Section 2, the Fourier modes again act independently of each other, and so can be considered separately. The linearized kinematic conditions (3.6) allow the coefficients $B_{n1}(t)$ and $C_{n1}(t)$ both to be eliminated in favour of $R_{n1}(t)$. Finally the dynamic condition (3.7) shows that, at the zeroth Fourier mode, the function $f_1(t)$ in the representation (3.11) must be given by the formula

$$f_1(t) = -\frac{1}{3}\omega_0^2 R_0^2(t).$$

After some algebra, it follows that the Fourier coefficients $\tilde{R}_{n1}(t)$ for the interface shape satisfy the identical second-order differential equation (2.16) as has already been encountered in Section 2, provided that $n \neq 2$. At the second Fourier-Legendre mode, however, the appropriate differential equation is found to be

$$\begin{aligned} &\frac{d^2\tilde{R}_{21}}{dt^2} R_0(2D+3) + \frac{d\tilde{R}_{21}}{dt}\frac{3(2D+3)}{4\pi R_0^2} \\ &-\tilde{R}_{21}\left[\frac{4(6-D)}{(4\pi)^2 R_0^5} + \frac{6(D-1)}{F^2 R_0^2}\right] = -2\omega_0^2 R_0^2 \\ &\quad \text{if } n = 2. \end{aligned} \tag{3.13}$$

The left-hand side of this equation is identical to (2.17), but the forcing term on the right-hand side is different in two significant ways. Firstly, it has the opposite sign from the straining case (2.17), and secondly, it involves a higher power of $R_0$. This equation (3.13) can be solved in closed form, similarly to equation (8.5) in the Appendix 8, but for general Froude number it is again difficult to see whether rotation is sufficient to force a bi-polar outflow in every case. However, for infinite Froude number, the situation is considerably clearer, and that special case is now considered separately.

## 3.1 Infinite Froude number limit

As for the corresponding case with straining flow, examined in section 2.1, the Froude number is here set to infinity, $F = \infty$, and represents the situation in which gravity is insignificant. The zeroth-order spherical radius $R_0$ in equation (2.8) is again taken as the independent variable, rather than the time $t$, and for every Fourier mode other than the second one ($n \neq 2$), the equation for the evolution of that mode is given by (2.18). Its solution (2.20) shows that the $n$-th Fourier-Legendre mode grows algebraically with time.

At the second mode, equation (3.13) in the infinite Froude-number limit becomes

$$R_0^2\frac{d^2\tilde{R}_{21}}{dR_0^2} + R_0\frac{d\tilde{R}_{21}}{dR_0} - \alpha_2^2\tilde{R}_{21} = -2\omega_0^2\frac{(4\pi)^2}{(2D+3)}R_0^7, \quad \text{for } n = 2, \tag{3.14}$$

in which the constant $\alpha_2$ is as given in equation (2.19). Equation (3.14) is an Euler-Cauchy differential equation, and its solution is easily calculated to be

$$\tilde{R}_{21}(R_0) = C_{21}R_0^{\alpha_2} + C_{22}R_0^{-\alpha_2} - \frac{2\omega_0^2(4\pi)^2}{3\big[34D+41\big]}R_0^7. \tag{3.15}$$

The two constants $C_{21}$ and $C_{22}$ are arbitrary.

This solution (3.15) has some similarities to the corresponding result (2.21) in the straining case; the second Fourier mode grows at the rate $R_0^7$ which always exceeds the growth rate $\sqrt{12/(D+2)}$ of the first mode. Therefore, rotation at any angular speed $\omega_0$ will ultimately cause the second mode to dominate, so that bi-polar outflow is the eventual result for infinite Froude number. However, since the sign of the last term in equation (3.15) is negative, then rotation is expected to give rise to solutions that are ultimately bi-polar, but that are *compressed* along the $z$-axis, with a corresponding expansion about their waists. This is unlike the straining situation in section 2.1, where positive strain rates caused an extension of the outflow bubble on the $z$-axis.

# 4 Boussinesq Model for Viscous Flow

Following Forbes (2011b), a viscous model for this outflow problem is now considered, based on the Boussinesq approximation in which it is assumed that the fluid density is continuous in space, instead of there being a density jump at an infinitessimally thin interface. This greatly simplifies the problem to be solved. In this approximation, the interface is represented as a narrow region across which the density changes smoothly but rapidly, producing a thin interfacial zone rather than a mathematical discontinuity. The problem is non-dimensionalized as in section 2, using the density ($\rho_1$) of the inner (lighter) fluid as the reference density. In dimensionless variables, the continuous density function is represented as $\rho = 1 + \bar{\rho}$ , and in the Boussinesq approximation, $\bar{\rho}$ is assumed to be small. Furthermore, this formulation "splits" the mass conservation equation into an incompressible component and a weakly compressible part that allows for the transport of the density variation function $\bar{\rho}$. This therefore gives the two equations

$$\begin{aligned} &\text{div}\mathbf{q} = 0 \\ &\frac{\partial \bar{\rho}}{\partial t} + \mathbf{q} \cdot \nabla \bar{\rho} = \sigma \nabla^2 \bar{\rho}. \end{aligned} \tag{4.1}$$

The dimensionless number $\sigma$ in the weakly compressible density transport equation is a diffusion constant, and is related to a Prandtl number. Further discussion may be found in the paper by Farrow and Hocking (2006). In the present paper, the quantity $\bar{\rho}$ is described as a perturbation density, with the result that the Boussinesq approximation treats the fluid as weakly compressible. However, if preferred, the perturbation density $\bar{\rho}$ can be eliminated in favour of some other quantity $\Theta$ through an effective equation of state, of the form

$$\bar{\rho} = -\alpha_S \Theta$$

in dimensionless variables. Here, $\Theta$ might represent the temperature rise above ambient (and $\alpha_S$ is a constant). In that case, the variable $\Theta$ still satisfies the second of the equations in the system (4.1), which would now correspond to an energy equation for the convection and diffusion of heat. The diffusion coefficient $\sigma$ then represents a coefficient of thermometric conductivity, as discussed by Chandrasekhar (1961, page 18) and Drazin and Reid (2004, page 37).

Although the geometry of this problem is assumed to remain axi-symmetric, provision is nevertheless made for a swirling component of velocity in the azimuthal ($\theta$) direction. Accordingly, the velocity vector is now written as

$$\mathbf{q} = u\mathbf{e_r} + w\mathbf{e}_\phi + v\mathbf{e}_\theta. \tag{4.2}$$

In the Boussinesq approximation, the Navier-Stokes equations of viscous fluid motion become

$$\frac{\partial \mathbf{q}}{\partial t} + \mathbf{q}\cdot\nabla\mathbf{q} + \nabla p = -\frac{1}{F^2}\left[\frac{1+\bar{\rho}}{r^2}\right]\mathbf{e_r} + \frac{1}{R_e}\nabla^2\mathbf{q}. \tag{4.3}$$

In this equation, $p$ represents the pressure, and $F$ is the Froude number based on the radially inward gravitational force, as in section 2. The additional parameter $R_e$ is a Reynolds number, and gives a measure of the inverse viscosity of the fluid. A source is present at the origin, within inner fluid 1, and it is represented as a mathematical point singularity. Provision is also made for solid-body rotation near the source, representing a spinning object at the origin. Consequently,

$$\mathbf{q} \to \frac{1}{4\pi r^2}\mathbf{e_r} + \omega r\sin\phi\mathbf{e}_\theta, \quad \text{as } r\to 0. \tag{4.4}$$

The additional parameter $\omega$ is the dimensionless angular speed of the rotating source in viscous fluid 1.

Since the geometry is assumed to be axi-symmetric, there is no dependence on the azimuthal coordinate, and consequently $\partial/\partial\theta \equiv 0$. The first equation in (4.1) therefore only involves the radial and axial fluid velocity components $u$ and $w$, and as a result, this equation can be satisfied identically by means of a streamfunction $\Psi$. It follows that

$$u = \frac{1}{r\sin\phi}\frac{\partial\big(\sin\phi\Psi\big)}{\partial\phi} \quad ; \quad w = -\frac{1}{r}\frac{\partial\big(r\Psi\big)}{\partial r}. \tag{4.5}$$

It is convenient now to consider the vorticity vector $\zeta = \mathrm{curl}\mathbf{q}$ , which in the

present problem takes the form

$$\begin{aligned}\zeta &= \frac{1}{r\sin\phi}\frac{\partial}{\partial\phi}\left(v\sin\phi\right)\mathbf{e_r} - \frac{1}{r}\frac{\partial}{\partial r}\left(rv\right)\mathbf{e}_\phi + Z\mathbf{e}_\theta \\ &\quad \text{where } Z = \frac{1}{r}\left[\frac{\partial}{\partial r}\left(rw\right) - \frac{\partial u}{\partial\phi}\right]. \end{aligned} \tag{4.6}$$

The component $Z$ of the vorticity in the azimuthal direction, in equation (4.6), can be expressed in terms of the streamfunction as a result of equation (4.5). The result is

$$Z(r,z,t) = -\left[\frac{1}{r^2}\frac{\partial}{\partial r}\left(r^2\frac{\partial\Psi}{\partial r}\right) + \frac{1}{r^2\sin\phi}\frac{\partial}{\partial\phi}\left(\sin\phi\frac{\partial\Psi}{\partial\phi}\right) - \frac{\Psi}{r^2\sin^2\phi}\right]. \tag{4.7}$$

The $r$- and $\phi$-components of the Boussinesq Navier-Stokes equations (4.3) are now combined to eliminate the pressure, which is equivalent to taking the vector curl of this equation and retaining only the azimuthal component. This gives a vorticity equation for the component $Z$. After some algebra, this becomes

$$\begin{aligned} &\frac{\partial Z}{\partial t} + u\frac{\partial Z}{\partial r} + \frac{w}{r}\frac{\partial Z}{\partial\phi} - \frac{Z}{r}\big(u + w\cot\phi\big) \\ + \;& \frac{2v}{r^2}\left(\frac{\partial v}{\partial\phi} - r\cot\phi\frac{\partial v}{\partial r}\right) - \frac{1}{F^2r^3}\frac{\partial\bar\rho}{\partial\phi} \\ = \;& \frac{1}{R_e}\left[\frac{1}{r^2}\frac{\partial}{\partial r}\left(r^2\frac{\partial Z}{\partial r}\right) + \frac{1}{r^2\sin\phi}\frac{\partial}{\partial\phi}\left(\sin\phi\frac{\partial Z}{\partial\phi}\right) - \frac{Z}{r^2\sin^2\phi}\right]. \end{aligned} \tag{4.8}$$

This must be solved in conjunction with the azimuthal component of the Navier-Stokes equations (4.3), which takes a somewhat similar form

$$\begin{aligned} &\frac{\partial v}{\partial t} + u\frac{\partial v}{\partial r} + \frac{w}{r}\frac{\partial v}{\partial\phi} + \frac{v}{r}\big(u + w\cot\phi\big) \\ = \;& \frac{1}{R_e}\left[\frac{1}{r^2}\frac{\partial}{\partial r}\left(r^2\frac{\partial v}{\partial r}\right) + \frac{1}{r^2\sin\phi}\frac{\partial}{\partial\phi}\left(\sin\phi\frac{\partial v}{\partial\phi}\right) - \frac{v}{r^2\sin^2\phi}\right]. \end{aligned} \tag{4.9}$$

Finally, the second of the equations in the system (4.1) must be included, and in this coordinate system it may be written out in full as

$$\begin{aligned} &\frac{\partial\bar\rho}{\partial t} + u\frac{\partial\bar\rho}{\partial r} + \frac{w}{r}\frac{\partial\bar\rho}{\partial\phi} \\ = \;& \sigma\left[\frac{1}{r^2}\frac{\partial}{\partial r}\left(r^2\frac{\partial\bar\rho}{\partial r}\right) + \frac{1}{r^2\sin\phi}\frac{\partial}{\partial\phi}\left(\sin\phi\frac{\partial\bar\rho}{\partial\phi}\right)\right]. \end{aligned} \tag{4.10}$$

These coupled equations are to be solved together with the condition (4.4) near the source at the origin. In addition, it is necessary in the solution method to create an artificial boundary $r = \beta$ at some distance from the source, to create an appropriate computational window. At that outer limit, the conditions

$$v = 0 \quad ; \quad \bar{\rho} = (D-1) \quad ; \quad u = \frac{1}{4\pi r^2} \quad \text{at } r = \beta \tag{4.11}$$

are imposed. This non-linear system of equations must be solved numerically, and this task is made potentially more difficult by the presence of a point singularity at the origin.

In view of the need to cope with this singularity, a spectral solution method is used for the solution of equations (4.8) – (4.10), following Forbes (2011b). The streamfunction in equations (4.5), (4.7) is represented in the form

$$\begin{aligned} \Psi(r,\phi,t) &= -\frac{\cot\phi}{4\pi r} + Ar^2\cos\phi\sin\phi \\ &+ \sum_{m=1}^{M}\sum_{n=1}^{N} B_{mn}(t)\frac{J_{n+1/2}\big(\alpha_{n,m}r\big)}{\sqrt{r}}P_n'(\cos\phi)\sin\phi. \end{aligned} \tag{4.12}$$

In this expression, $P_n$ are the Legendre polynomials, as in section 2, and $J_{n+1/2}$ are the Bessel functions of first kind, of half-fractional order. The constant $A$ is the strain rate parameter. In addition, the constants

$$\alpha_{n,m} = j_{n+1/2,m}/\beta \tag{4.13}$$

have been defined. The symbol $j_{\nu,s}$ denotes the $s$-th zero of the Bessel function of order $\nu$, consistently with the notation of Abramowitz and Stegun (1972, page 370). The radial and axial components of the velocity vector $\mathbf{q}$ can now be computed from equation (4.12) using (4.5), and the result is

$$\begin{aligned} u(r,\phi,t) &= \frac{1}{4\pi r^2} + Ar\big(3\cos^2\phi - 1\big) \\ &+ \sum_{m=1}^{M}\sum_{n=1}^{N} n(n+1)B_{mn}(t)\frac{J_{n+1/2}\big(\alpha_{n,m}r\big)}{r^{3/2}}P_n(\cos\phi) \end{aligned} \tag{4.14}$$

and

$$\begin{aligned} w(r,\phi,t) &= -3Ar\cos\phi\sin\phi - \sum_{m=1}^{M}\sum_{n=1}^{N} B_{mn}(t)\Big[\tfrac{1}{2}r^{-3/2}J_{n+1/2}\big(\alpha_{n,m}r\big) \\ &+ \alpha_{n,m}r^{-1/2}J_{n+1/2}'\big(\alpha_{n,m}r\big)\Big]P_n'(\cos\phi)\sin\phi. \end{aligned} \tag{4.15}$$

The streamfunction can also be used to obtain the azimuthal component of the vorticity vector (4.6). An additional advantage of this spectral method is that the Poisson equation (4.7) leads at once to

$$Z(r,\phi,t) = \sum_{m=1}^{M}\sum_{n=1}^{N} \alpha_{n,m}^2 B_{mn}(t) \frac{J_{n+1/2}\big(\alpha_{n,m}r\big)}{\sqrt{r}} P_n'(\cos\phi)\sin\phi, \tag{4.16}$$

without numerical approximation.

The perturbed density function is likewise represented spectrally, and the form taken by Forbes (2011b) is available here also. Thus

$$\begin{aligned} \bar{\rho}(r,\phi,t) &= (D-1)\left(\frac{r}{\beta}\right)^3 + \sum_{m=1}^{M} C_{m0}(t)\sin\left(\frac{m\pi r^3}{\beta^3}\right) \\ &+ \sum_{m=1}^{M}\sum_{n=1}^{N} C_{mn}(t) r^{5/2} J_{n+1/2}\big(\alpha_{n,m}r\big) P_n(\cos\phi), \end{aligned} \tag{4.17}$$

with the constants $\alpha_{n,m}$ again given by equation (4.13). This follows from a careful analysis of the forms of the functions needed to satisfy the vorticity equation (4.8). The streamfunction (4.12) and density (4.17) obey the requirements (4.4) and (4.11) at the boundaries of the computational domain.

Finally, a representation is needed for the azimuthal component $v$ in the velocity vector (4.2). To begin, a background field

$$v^S(r,\phi) = \begin{cases} \omega r\sin\phi, & 0<r<1 \\ 0, & 1<r<\beta \end{cases} \tag{4.18}$$

is considered, representing solid-body rotation in the unit sphere occupied by inner fluid 1 at initial time $t=0$. This is now represented spectrally, in the form

$$v^S(r,\phi) = \sum_{m=1}^{M} V_{m0}^S \frac{J_{3/2}\big(\alpha_{1,m}r\big)}{\sqrt{r}}\sin\phi,$$

and decomposed into its Fourier-Bessel modes using the orthogonality relation

$$\int_0^\beta r J_{\ell+1/2}\big(\alpha_{\ell,m}r\big) J_{\ell+1/2}\big(\alpha_{\ell,k}r\big)\,dr = \begin{cases} 0, & m\neq k \\ (\beta^2/2) J_{\ell+3/2}^2\big(\alpha_{\ell,k}\beta\big), & m=k \end{cases} \tag{4.19}$$

for the half-order Bessel functions of the first kind. Equation (4.19) may be obtained from Gradshteyn and Ryzhik (2000, page 658), and it yields

$$V_{k0}^S(\beta^2/2) J_{5/2}^2\big(\alpha_{1,k}\beta\big) = \omega\int_0^1 r^{5/2} J_{3/2}\big(\alpha_{1,k}r\big)\,dr.$$

The integral on the right-hand side of this expression can be evaluated in closed form, using an identity from Abramowitz and Stegun (1972, page 361). Consequently,

$$V_{m0}^S = \frac{2\omega J_{5/2}\big(\alpha_{1,m}\big)}{\alpha_{1,m}\beta^2 J_{5/2}^2\big(\alpha_{1,m}\beta\big)}. \tag{4.20}$$

This background flow is used to create a representation for the azimuthal component of the velocity vector, in the form

$$\begin{aligned} v(r,\phi,t) &= \sum_{m=1}^{M} V_{m0}^S \frac{J_{3/2}\big(\alpha_{1,m}r\big)}{\sqrt{r}} \sin\phi \\ &+ \sum_{m=1}^{M}\sum_{n=1}^{N} V_{mn}(t) \frac{J_{n+1/2}\big(\alpha_{n,m}r\big)}{\sqrt{r}} P_n'(\cos\phi)\sin\phi, \end{aligned} \tag{4.21}$$

with the constants $V_{m0}^S$ given in equation (4.20).

As yet, the three sets of Fourier coefficients $B_{mn}(t)$ , $C_{mn}(t)$ , $V_{mn}(t)$ are unknown. They must be obtained from the three equations (4.8) – (4.10). These equations are spectrally decomposed, using the orthogonality relation (4.19) for Bessel functions, along with the results

$$\int_0^\pi P_n(\cos\phi)P_\ell(\cos\phi)\sin\phi\, d\phi = \begin{cases} 0, & n \neq \ell \\ 2/(2\ell+1), & n = \ell \end{cases} \tag{4.22}$$

and

$$\int_0^\pi P_n'(\cos\phi)P_\ell'(\cos\phi)\sin^3\phi\, d\phi = \begin{cases} 0, & n \neq \ell \\ 2\ell(\ell+1)/(2\ell+1), & n = \ell \end{cases}. \tag{4.23}$$

Equation (4.22) is the usual orthogonality result for Legendre polynomials, and (4.23) is a similar result for the derivatives of these polynomials; it may be derived from an identity for associated Legendre polynomials given by Abramowitz and Stegun (1972, page 338). It is most efficient to compute the Legendre functions $P_n(\cos\phi)$ and their derivatives $P_n'(\cos\phi)$ from three-term recurrence relations, and these are presented in Forbes (2011b). These functions are calculated once, stored, and not re-computed.

The vorticity equation (4.8) is multiplied by $P_\ell'(\cos\phi)\sin^2\phi$ and integrated over the interval $0 < \phi < \pi$. The orthogonality relation (4.23) is then used to evaluate the appropriate integrals. The result is next multiplied by the quantity $r^{3/2}J_{\ell+1/2}\big(\alpha_{\ell,k}r\big)$ and integrated over $r$, making use of the relation (4.19) for Bessel functions. After some algebra, this gives rise to a system of $MN$ ordinary differential equations for the Fourier coefficients

$B_{k\ell}(t)$ , which for completeness are presented in Appendix B (Sec. 9). The azimuthal component (4.9) of the Boussinesq Navier-Stokes equation has the similar structure, and so it is treated in the same way as the vorticity equation. Again, a system of $MN$ differential equations for the coefficients $V_{mn}(t)$ is obtained, and these, too, are given in Appendix B (Sec. 9).

Finally, the density equation (4.10) is similarly subject to Fourier decomposition. To begin, it is multiplied by $\sin\phi$ and integrated, making use of (4.22). The resulting expression is then further multiplied by $r^2\sin\bigl(k\pi r^3/\beta^3\bigr)$ and integrated with respect to $r$. This gives a system of ordinary differential equations for the zeroth-order coefficients $C_{m0}(t)$ . The higher-order Fourier modes are next obtained at the $\ell$-th order in $\phi$ by multiplying (4.10) by $P_\ell(\cos\phi)\sin\phi$ and integrating over the interval $0<\phi<\pi$. The resulting equation is multiplied by $r^{-3/2}J_{\ell+1/2}\bigl(\alpha_{\ell,k}r\bigr)$ and integrated, using the orthogonality relation (4.19) to evaluate the integrals. This gives the final system of $MN$ differential equations for $C_{mn}(t)$. These are also presented in Appendix B (Sec. 9).

It remains to specify initial conditions for the flow. Since the initial conditions for the azimuthal component of the velocity are just those in the background flow (4.18), the coefficients are set to the values $V_{mn}(0)=0$ at time $t=0$. The flow is started with a spherical interface of unit radius, as in section 2, so that the density perturbation is taken to be

$$\bar\rho(r,\phi,0)=\begin{cases}0 & \text{for } 0<r<1\\ D-1 & \text{for } 1<r<\beta,\end{cases}$$

at time $t=0$. Following Forbes (2011b), this equation combined with (4.17) gives

$$\begin{aligned}C_{k0}(0) &= \frac{2(D-1)}{k\pi}\cos\bigl(k\pi/\beta^3\bigr)\\ C_{k\ell}(0) &= 0,\quad k=1,2,\ldots,M\quad \ell=1,2,\ldots,N.\end{aligned}$$

Again following Forbes (2011b), it will be assumed here that an initial perturbation with amplitude $\epsilon$ is made to the radial velocity component at the $n$-th spherical mode, at time $t=0$. Thus

$$u(r,\phi,0)=\frac{1}{4\pi r^2}+\begin{cases}\epsilon r^{n-1}P_n(\cos\phi) & \text{for } 0<r<1\\ \epsilon r^{-n-2}P_n(\cos\phi) & \text{for } 1<r<\beta\end{cases}\qquad(4.24)$$

for some particular $n$, which mimics the corresponding inviscid case (2.9). It

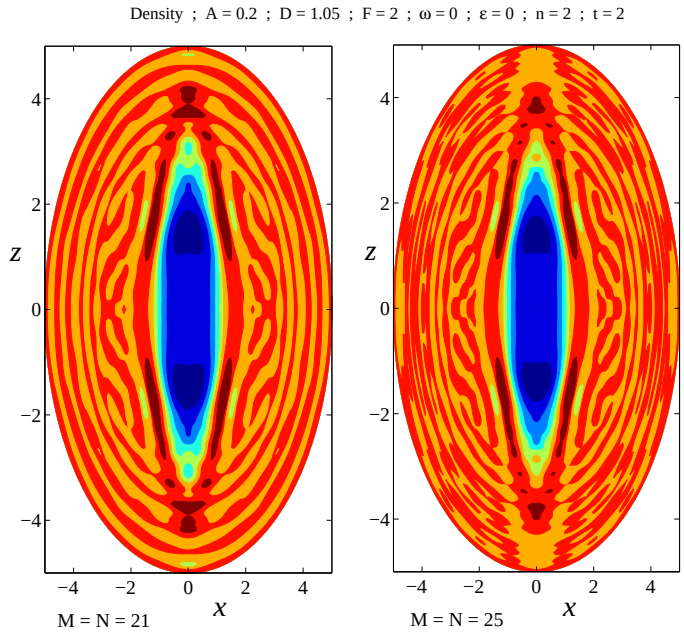


Figure 2: Density contours for viscous solutions with strain rate $A = 0.2$ at the second mode $n = 2$, for Froude number $F = 2$ and density ratio $D = 1.05$. There is no rotation, $\omega = 0$, and no initial disturbance, $\epsilon = 0$. Solutions have been obtained with two different numbers of Fourier coefficients, $M = N = 21$ (left picture) and $M = N = 25$ (right picture).

follows from equation (4.14) that $B_{k\ell} = 0$ for $\ell \neq n$, but that

$$B_{kn}(0) = \frac{2\epsilon}{n(n+1)\alpha_{n,k}\beta^2 J^2_{n+3/2}\big(\alpha_{n,k}\beta\big)}\left[\frac{(2n+1)}{\alpha_{n,k}}J_{n+1/2}\big(\alpha_{n,k}\big) - \frac{J_{n-1/2}\big(\alpha_{n,k}\beta\big)}{\beta^{n-1/2}}\right],$$

for the special case $\ell = n$.

The equations given in Appendix B (Sec. 9) represent a coupled system of $M(3N+1)$ ordinary differential equations for the Fourier coefficients. These are to be solved subject to the initial conditions given above, although a variation of this starting flow will also be considered later. The integrals in the equations in Appendix B (Sec. 9) are evaluated with Gauss-Legendre quadrature, using the algorithm provided by von Winckel (2004). This is carried out with 161 mesh points in each coordinate, over the computational window $0 < r < \beta$, $0 < \phi < \pi$, and in the results to be presented here, the artificial boundary $r = \beta$ is chosen to be located at $\beta = 5$. Gaussian

quadrature of order 161 is so accurate as to be essentially exact in this application, so that the numerical error comes from truncating the series at the $(M, N)$-th Fourier mode. An example solution is shown in Figure 2 for an outflow generated by straining motion, and computed with the two different numbers of Fourier coefficients $M = N = 21$ and $M = N = 25$ in each of the two coordinate variables $r$ and $\phi$. It has been found in this work that 25 coefficients is sufficient to resolve all the features of these flows, except occasionally for very fine details near the heads of outflow jets. This may perhaps be visible in Figure 2. Accordingly, results are presented here with $M = N = 25$ coefficients. The differential equations in Appendix B (Sec. 9) for these Fourier coefficients are integrated forward in time using the *MATLAB* routine *ode45*, which is an implementation of a fourth-fifth-order Runge-Kutta-Fehlberg algorithm with adaptive time steps to control the error. The computer run time is of the order of five hours on a standard quad-core personal computer.

# 5 Presentation of Results

The linearized solutions of Section 2 showed that, for infinite Froude number $F \to \infty$, the the first spherical mode was the most unstable and grew at the fastest rate. However, when a straining flow was then added, the *second* mode now became the most unstable and had the fastest growth rate. In that case, straining was sufficient to convert the one-sided outflow jet into a bipolar outflow. However, at finite values of the Froude number $F$ the situation is less clear, and it appears that, in general, this situation does not continue to be the case, so that even in the presence of straining, a one-sided jet is the most likely outcome. Nevertheless, these conclusions were based on the assumption that the interface shape consisted of only small perturbations to the unit sphere (in dimensionless variables), so that the strain rate parameter $A$ was necessarily required to be small. The first question to be asked of a numerical solution to the full non-linear problem, in which $A$ is now allowed to be of arbitrary size, is whether sufficiently large strain rates can produce bipolar outflows once again.

Figure 3 shows solutions at two different times $t = 0.6$ and $t = 1.2$, for a small strain rate $A = 0.1$. There is no rotation ($\omega = 0$) and the Froude number has the moderate value $F = 2$. Initially, a perturbation was made to the radial velocity component $u$ with amplitude $\epsilon = 0.1$ and at the lowest spherical mode $n = 1$. The linearized solution of section 2 suggests that the lowest mode is likely still to be the most unstable one, and this is confirmed by the two solutions shown in Figure 3. Here, shaded contours of the density

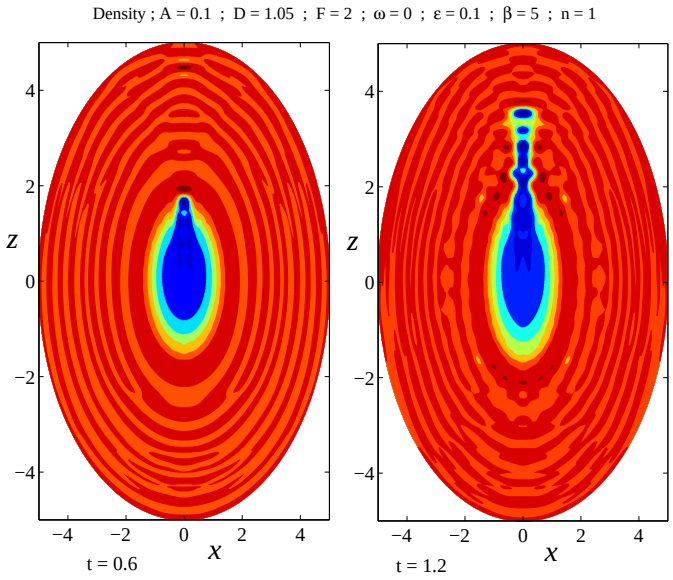


Figure 3: Density contours for viscous solutions with strain rate $A = 0.1$ at the first mode $n = 1$, for Froude number $F = 2$ and density ratio $D = 1.05$. There is no rotation, $\omega = 0$, and the initial amplitude was $\epsilon = 0.1$. Solutions are shown at the two times $t = 0.6$ and 1.2.

perturbation function $\bar{\rho}$ are drawn. The density ratio in this case is $D = 1.05$ and outside the expanding bubble the solution is very nearly uniform at the value $\bar{\rho} = 0.05$, as expected. There are, in fact, very small oscillations about this value as a result of Gibbs' phenomenon (see Kreyszig 2011), but these are of no consequence; nevertheless, they may be visible in the diagrams. Inside the expanding bubble, the perturbation density is $\bar{\rho} = 0$, again as expected, and there is a narrow region across which $\bar{\rho}$ changes rapidly but smoothly from one value to the other. This defines the effective interface zone. At the earlier time $t = 0.6$, the expanding bubble still retains its approximately spherical shape, although there is a small jet beginning to form at the "upper" pole of the sphere. (Since gravity is directed radially inward, there is no true "up" or "down" in these diagrams, and in fact the jet can form at either pole; the one at which it develops is determined by details of the numerical solution). By the later time $t = 1.2$ a strong one-sided jet has developed at that same pole, and is clearly visible in the upper portion of the diagram. In this case, straining is insufficient to make a qualitative change to the morphology of the outflow.

The solution of Figure 3 has been repeated in Figure 4, but now for the larger strain rate $A = 0.5$. Contours of the perturbation density $\bar{\rho}$ are again

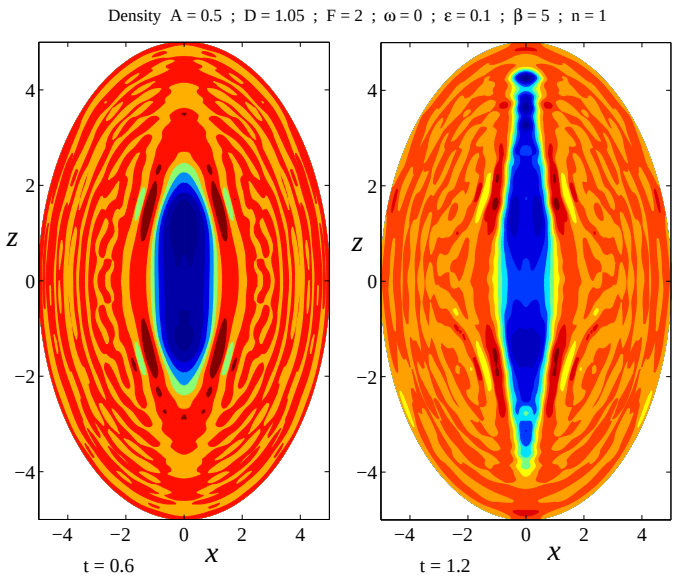


Figure 4: Density contours for viscous solutions with strain rate $A = 0.5$ at the first mode $n = 1$, for Froude number $F = 2$ and density ratio $D = 1.05$. There is no rotation, $\omega = 0$, and the initial amplitude was $\epsilon = 0.1$. Solutions are shown at the two times $t = 0.6$ and 1.2.

displayed at the same two times $t = 0.6$ and $t = 1.2$, and the interfacial zone is clearly evident as a narrow region in which $\bar{\rho}$ changes from zero near the origin to the value 0.05 in the outer zone. It is immediately clear in this case that the higher strain rate $A = 0.5$ is now responsible for converting the one-sided jet into an essentially bipolar outflow, even although the initial perturbation was made to the lowest mode $n = 1$. A close examination of the outflow at the later time $t = 1.2$ reveals that it is not precisely symmetric about the midplane $z = 0$, but it is nevertheless now strongly bipolar. Interestingly, there are narrow regions in the outer fluid at about $z = \pm 2$ where the density rises above the ambient value $D = 1.05$, due to the compressive effects associated with the straining motion about the interface. (Alternatively, these regions may be regarded as zones of elevated temperature in this Boussinesq approach, as indicated in the discussion following equation 4.1). These appear as four small regions at about $z = \pm 2$ in Figure 4, particularly at the later time $t = 1.2$, since these are effectively cross-sections through the flow on the plane $y = 0$.

To assist in visualizing the outflows obtained at the two different straining rates in Figures 3 and 4, the effective interface has been created from the density profile $\bar{\rho} = 0.03$, approximately in the middle of the interfacial zone.

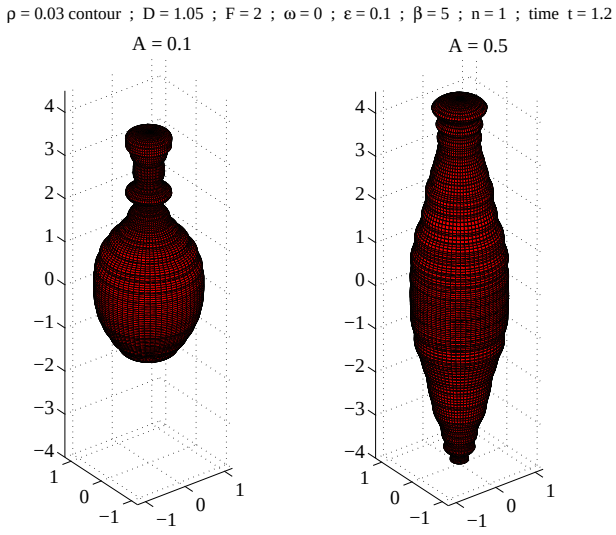


Figure 5: The axi-symmetric interface shape created from the density contour $\bar{\rho} = 0.03$ at time $t = 1.2$. Results are shown for the two different strain rates $A = 0.1$ and $A = 0.5$. The remaining parameters are as for Figures 3 and 4.

Results are shown in Figure 5, at the time $t = 1.2$ (the later time in the previous two Figures), but for the two different strain rates $A = 0.1$ and $A = 0.5$. In Figure 5, the scale on all the axes is the same, so that the outflow is as it would actually appear. For the smaller strain rate $A = 0.1$, the picture on the left shows a nearly spherical bubble with a one-sided outflow, and this is similar in morphology to the outflows shown by Forbes (2011b) for which no strain was present at all. However, in the picture on the right, the interface at the larger strain rate $A = 0.5$ has been pulled into an elongated shape, with a wider waist but with strong outflow jets from each pole. These jets are nevertheless not entirely symmetric, so that hints of the one-sided nature of the flow still persist.

It is now of interest to see the effect that pure rotation has upon outflow morphologies. An interesting case is portrayed in Figure 6. This is a solution started by a perturbation of amplitude $\epsilon = 0.1$ at the second mode $n = 2$, for density ratio $D = 1.05$ and the smaller Froude number $F = 0.5$, representing a rather more massive object at the origin. There is no straining in this case, so that $A = 0$, and the interface has been re-created from the $\bar{\rho} = 0.02$ contour approximately in the middle of the interfacial zone for this solution. The interface is displayed at time $t = 4$. The spinning motion is evidently responsible for the appearance of a pronounced waist-band near the plane $z = 0$. There is outflow from each pole, so that the solution is bipolar to a

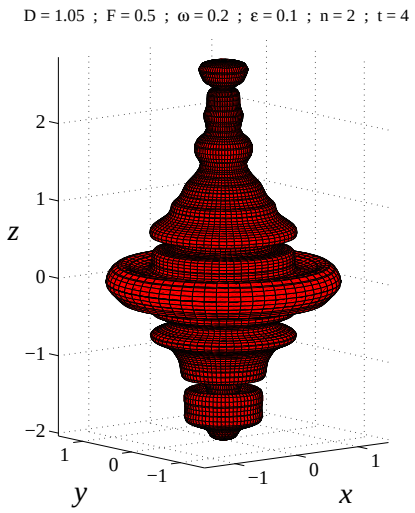


Figure 6: An axi-symmetric interface shape created from the density contour $\bar{\rho} = 0.02$, for a viscous solution with rotation speed $\omega = 0.2$ at the second mode $n = 2$, for Froude number $F = 0.5$ and density ratio $D = 1.05$. There is no straining flow, $A = 0$, and the initial amplitude was $\epsilon = 0.1$. The solution is shown at time $t = 4$.

large degree, although again the two jets are not symmetric, even although the solution was started from a perturbation to the second mode $n = 2$ only. In addition, each outflow jet has created an over-turning interface, and the plume at the lower side of the picture has generated quite a pronounced over-hanging plume near its head.

Figure 7 gives a further direct comparison of the effects of rotation on the outflow shape. Here, the interface has been created using the contour $\bar{\rho} = 0.02$ of the perturbed density function, and solutions are shown for the case of no rotation, $\omega = 0$, and a strong rotation $\omega = 3$. In this example, there is a weak straining flow with $A = 0.1$, the Froude number is $F = 2$ and the density ratio is $D = 1.05$. Both of these solutions were generated from perturbations to the first, most unstable, mode $n = 1$ and both are shown at the same time $t = 1.2$.

The solution on the left of this diagram represents the case of no rotation, and consists of a one-sided jet exiting the pole of the sphere at the top of the picture. This is the same case as depicted for the left-hand picture in Figure 5. (In this diagram the contour $\bar{\rho} = 0.02$ has been used to create the interface, whereas in Figure 5 the contour $\bar{\rho} = 0.03$ was used. Nevertheless, the two images are very similar, because the contours in the interfacial zone are packed closely together in this narrow region). By contrast, the solution

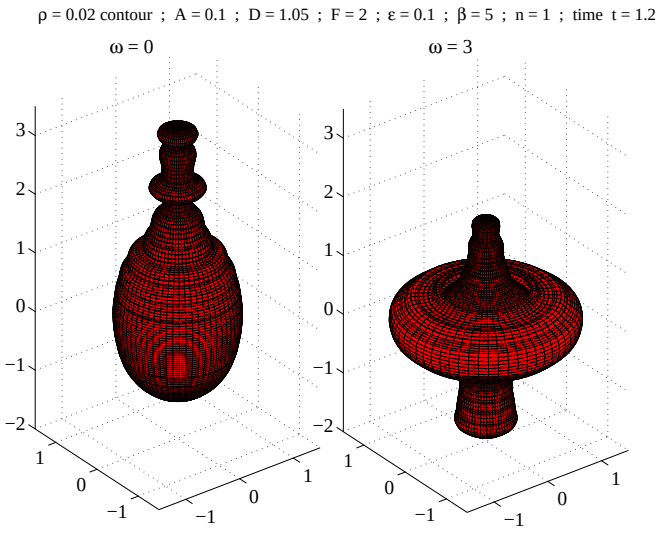


Figure 7: The axi-symmetric interface shape created from the density contour $\bar{\rho} = 0.02$ at time $t = 1.2$. Results are shown for the two different rotation speeds $\omega = 0$ (no rotation) and $\omega = 3$. The strain rate is $A = 0.1$ for a perturbation at the first mode $n = 1$ with amplitude $\epsilon = 0.1$, with Froude number $F = 2$ and density ratio $D = 1.05$.

shown on the right of Figure 7 is no longer a one-sided outflow, but now consists of outflow jets from both of the poles of the sphere. However, the outflow jets are again not exactly symmetric about the mid-plane $z = 0$. In addition, there is again a strong waistband structure in the morphology of the interface for the $\omega = 3$ case, including some small regions of over-hang. This is consistent with the weakly non-linear analysis of Section 3, which suggests that the outflow is reduced along the $z$-axis, although still bi-polar, with a corresponding expansion in the region of the waist. For both diagrams in Figure 7, the scale is the same on all axes, so that these two shapes are as they would actually appear, and are both drawn to the same scale.

Figure 8 shows the development of the azimuthal velocity component $v$, for the strongly rotating solution $\omega = 3$ depicted on the right side of Figure 7. Two solutions are shown here, at the times $t = 0.2$ and $t = 1.2$. These are first-mode solutions with $n = 1$, and the remaining parameters are as in Figure 7. Contours of the azimuthal speed $v$ are presented, and only the portion of the solution in the region $-2 < x < 2$, $-2 < z < 2$ is shown, for ease of viewing. These diagrams illustrate the decay of the rotational component with time. At the time $t = 0.2$ shown in Figure 8(a), the speed $v$ is essentially zero outside the initial unit sphere, and at this early time, there is a maximum of about $|v| = 2.5$ in a small region close to the centre-plane $z = 0$. Notice that the initial discontinuity in the speed profile (4.18) at $r = 1$ soon develops into a thin region in which $v$ changes rapidly but smoothly, and this is evident in Figure 8(a) at this early time $t = 0.2$. As time progresses, the azimuthal speed $v$ reduces in magnitude, and becomes more focussed, so that, by time $t = 1.2$ shown in Figure 8(b), almost all the rotational motion is confined within the waistband structure shown in the right-hand diagram of Figure 7. Furthermore, the magnitude of this quantity has approximately halved. Interestingly, the two outflow jets shown in Figure 7 are not associated with any significant amount of rotational motion, as is evident from the contours in Figure 8(b).

As a further aid to visualizing the evolution of the solution in Figure 8, it is instructive to draw the instantaneous stream-surfaces. From Batchelor (1967), streamlines are curves which are parallel to the velocity vector $\mathbf{q}$ in equation (4.2). In spherical polar coordinates (2.1), it is possible to show that one family of stream-surfaces is given by the equation $r \sin \phi \Psi = \text{constant}$, at least in steady flow. Accordingly, this quantity has been calculated from the spectral representation (4.12), and cross-sections of these surfaces have been plotted in the $x$-$z$ plane using a contouring routine. These are shown in Figures 9. In these diagrams, the full computational window $0 < r < \beta = 5$ is shown, and the scales are the same on both pairs of axes.

In the outer field, the stream-surfaces far from the origin remain essen-

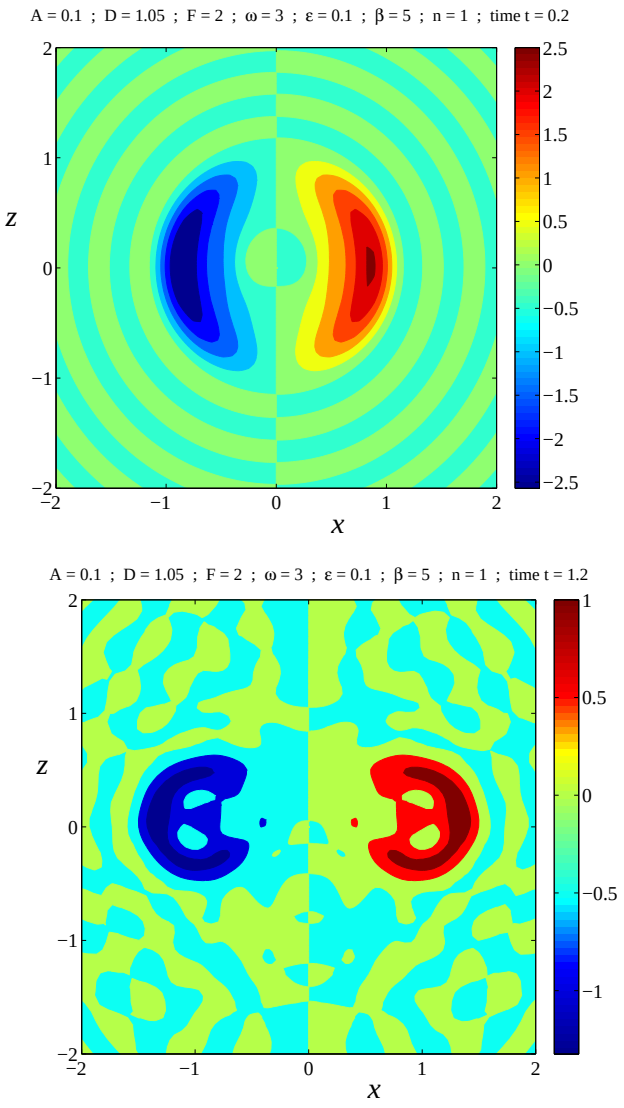


Figure 8: Evolution of the azimuthal velocity component $v$ for a solution with strain rate $A = 0.1$ and rotational speed $\omega = 3$. The scales on both axes are the same. The density ratio is $D = 1.05$ and the Froude number is $F = 2$. The initial perturbation was to the $n = 1$ mode. Solutions are shown at times (a) $t = 0.2$ and (b) $t = 1.2$.

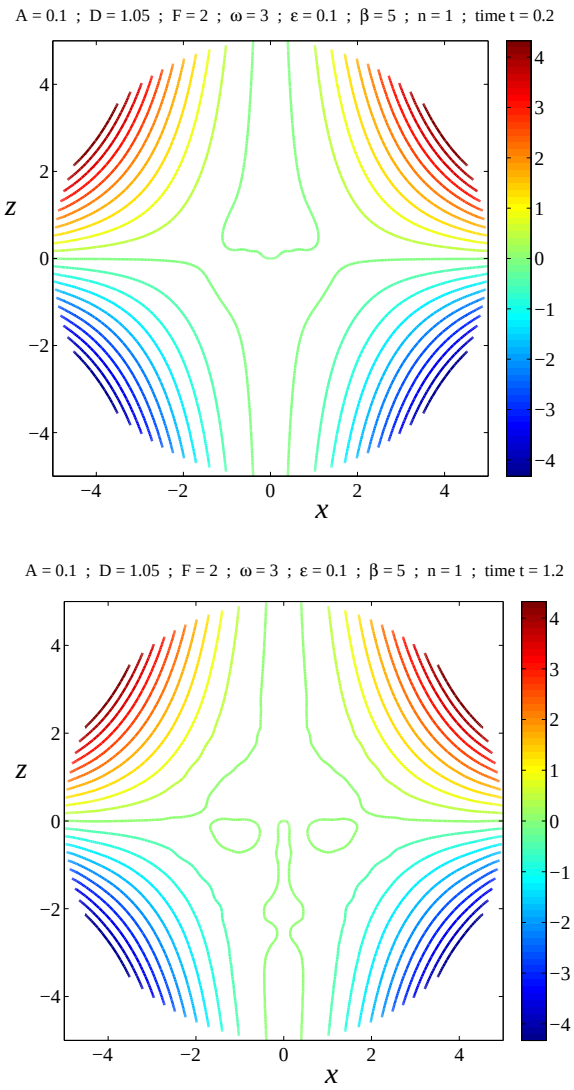


Figure 9: Streamlines for a solution with strain rate $A = 0.1$ and rotational speed $\omega = 3$. The scales on both axes are the same. The density ratio is $D = 1.05$ and the Froude number is $F = 2$. The initial perturbation was to the $n = 1$ mode. Solutions are shown at times (a) $t = 0.2$ and (b) $t = 1.2$.

tially unchanged as time progresses, as can be seen by comparing Figure 9(a) at the early time $t = 0.2$ with the later time $t = 1.2$ shown in Figure 9(b). They have a roughly hyperbolic shape, as is to be expected from the straining motion in equation (2.5). In the near-field close to the origin, there is a widening of the region at the bottom of the diagram, and this is associated with the outflow jet that can be seen at the bottom of the right-hand picture in Figure 7.

Finally, the azimuthal component $Z$ of the vorticity has been calculated for this same case shown in Figures 8 and 9, from the spectral representation (4.16) of this function. Contours of the vorticity component $Z$ are shown in Figure 10(a) at time $t = 0.2$, and Figure 10(b) shows $Z$ at the later time $t = 1.2$. For ease of viewing, only the section $-3 < x < 3$, $-3 < z < 3$ is displayed here, and the scale on the axes is the same. For the pure background flow (2.5) consisting only of spherical outflow and the straining field, the vorticity component $Z$ is zero everywhere, except at the origin where it is infinite. Thus at the early time $t = 0.2$ shown in Figure 10(a) the azimuthal vorticity $Z$ is essentially zero everywhere, except for a small intense patch near the origin. However at the later time $t = 1.2$ in Figure 10(b), while the azimuthal vorticity is zero almost everywhere, there is nevertheless an intense patch near the $z$-axis at the bottom of the diagram, associated with the strong jet out of the lower pole in the right-hand side picture in Figure 7. In addition, there is a smaller patch of vorticity component $Z$ near the head of the upper-most jet.

Figures 8 – 10 therefore create an interesting account of the development of the solution at rotation rate $\omega = 3$ shown on the right-hand side of Figure 7. The combination of straining and rotation causes what would otherwise have been a one-sided jet to be replaced instead with the bipolar morphology in Figure 7, with a pronounced waistband structure and jets emerging from both poles of the sphere. As the outflow evolves in time, the energy within the rotational component $v$ of the velocity vector decays, and what remains is concentrated in the waistband near the centre-plane $z = 0$. This is partly due to viscosity and diffusion, but it is evidently the case also that the energy associated with the azimuthal speed $v$ in the outflow jets is diverted in large measure into rotation in the plane $\left(\mathbf{e_r}, \mathbf{e}_\phi\right)$ orthogonal to the azimuthal direction. This is visible as the intense patch of vorticity component $Z$ particularly in the jet from the lower pole in these diagrams.

To conclude this presentation of results, it is interesting to consider an initial condition that involves all the Fourier modes, instead of just a monochromatic disturbance at the $n$-th mode only. To this end, the initial radial

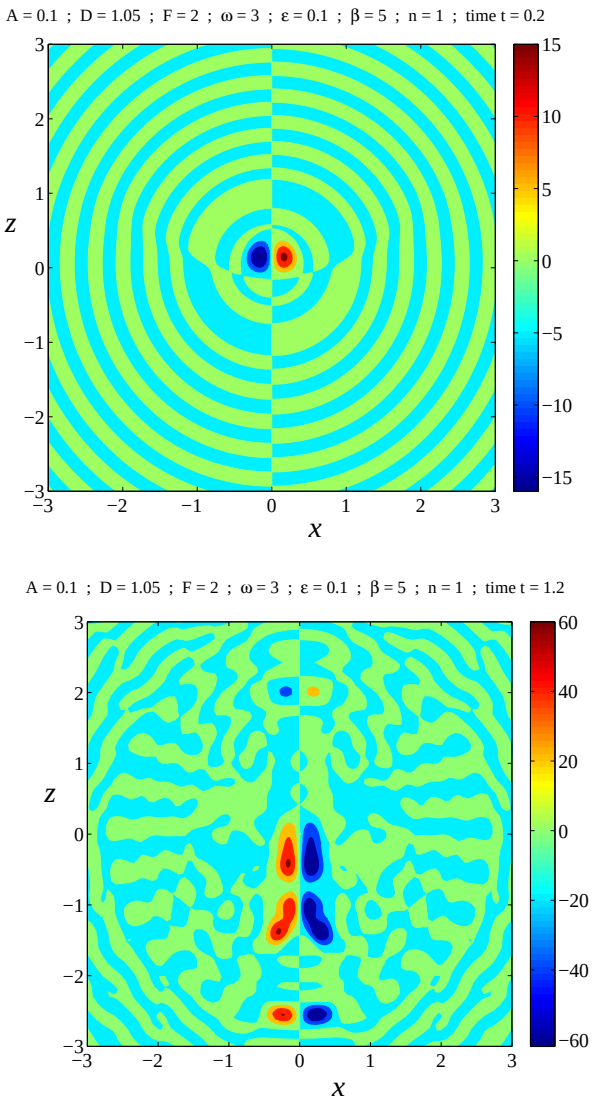


Figure 10: Contours of the azimuthal component $Z$ of the vorticity, for a solution with strain rate $A = 0.1$ and rotational speed $\omega = 3$. The scales on both axes are the same. The density ratio is $D = 1.05$ and the Froude number is $F = 2$. The initial perturbation was to the $n = 1$ mode. Solutions are shown at times (a) $t = 0.2$ and (b) $t = 1.2$.

velocity profile (4.24) in now replaced with the multi-modal disturbance

$$u(r,\phi,0) = \frac{1}{4\pi r^2} + \begin{cases} \sum_{n=1}^{N} B_n^{IN} r^{n-1} P_n(\cos\phi) & \text{for } 0 < r < 1 \\ \sum_{n=1}^{N} B_n^{IN} r^{-n-2} P_n(\cos\phi) & \text{for } 1 < r < \beta. \end{cases} \tag{5.1}$$

Now the new coefficients $B_n^{IN}$ in this initial condition (5.1) will be chosen so that initially, and on the surface $r = 1$ of the sphere of inner fluid, the radial velocity component behaves as

$$u(1,\phi,0) = \begin{cases} \big(2\epsilon/\pi\big)\phi & \text{for } 0 < \phi < \pi/2 \\ \big(2\epsilon/\pi\big)(\pi - \phi) & \text{for } \pi/2 < \phi < \pi. \end{cases} \tag{5.2}$$

It now follows from equation (5.1) and the orthogonality condition (4.22) that the coefficients for this new initial condition are obtained from (5.2) in the form

$$B_\ell^{IN} = \frac{2\ell+1}{2} \int_0^\pi u(1,\phi,0) P_\ell(\cos\phi) \sin\phi \, d\phi, \quad \ell = 1, \ldots, N \tag{5.3}$$

and these quadratures are evaluated using the Gaussian routine of von Winckel (2004). Finally, the representation (4.14) of the radial velocity component is evaluated at $t = 0$ and compared with the initial condition (5.1). The orthogonality conditions (4.22), (4.19) are used to give the initial values of the Fourier coefficients $B_{mn}$ in the form

$$\begin{aligned} B_{k\ell}(0) \;\; = \;\; & \frac{(2\ell+1)}{\ell(\ell+1)\beta^2 J_{\ell+3/2}^2\big(\alpha_{\ell,k}\beta\big)} \int_0^\beta \int_0^\pi r^{5/2} J_{\ell+1/2}\big(\alpha_{\ell,k} r\big) \\ & \times u(r,\phi,0) P_\ell(\cos\phi) \sin\phi \, d\phi \, dr. \end{aligned}$$

In this expression, the strain has been ignored, $A = 0$, for simplicity. It turns out that the integrals in this equation can all be evaluated in closed form, giving

$$\begin{aligned} B_{k\ell}(0) \;\; = \;\; & \frac{2B_\ell^{IN}}{\ell(\ell+1)\alpha_{\ell,k}\beta^2 J_{\ell+3/2}^2\big(\alpha_{\ell,k}\beta\big)} \Big[ J_{\ell+1/2}\big(\alpha_{\ell,k}\big) \\ & + J_{\ell-1/2}\big(\alpha_{\ell,k}\big) - \beta^{1/2-\ell} J_{\ell-1/2}\big(\alpha_{\ell,k}\beta\big) \Big] \end{aligned}$$

after some algebra. The coefficients $B_\ell^{IN}$ are obtained from (5.3).

The development of an outflow starting from this multi-modal initial disturbance is shown in Figure 11. There is no straining flow in this solution,

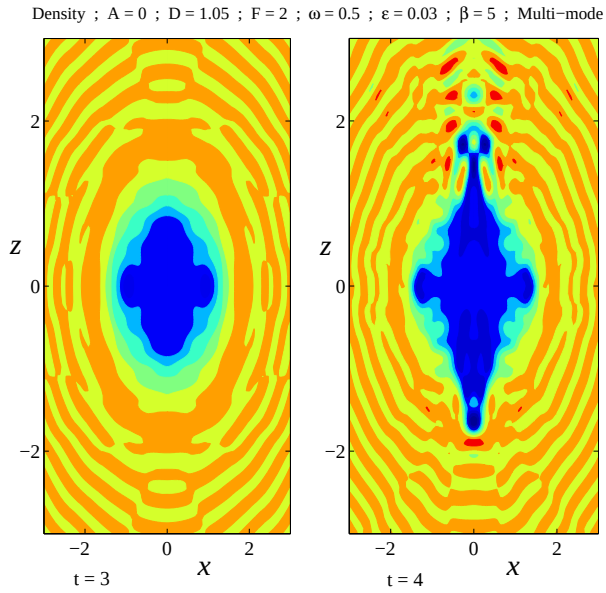


Figure 11: Density contours for viscous solutions with no background strain, $A = 0$, for the multi-modal initial condition. The density ratio is $D = 1.05$ and the Froude number is $F = 2$. The angular speed is $\omega = 0.5$ and the initial amplitude was $\epsilon = 0.03$. Solutions are shown at the two times $t = 3$ and 4.

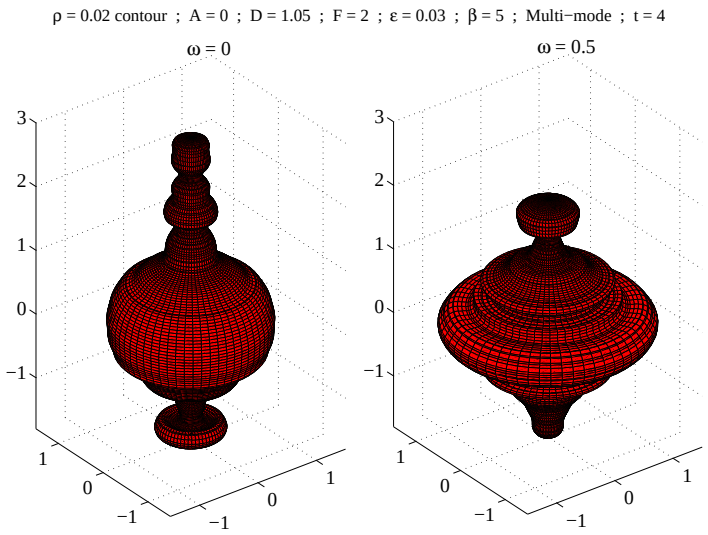


Figure 12: The axi-symmetric interface shape created from the density contour $\bar{\rho} = 0.02$ at time $t = 4$. Results are shown for the two different rotation speeds $\omega = 0$ (no rotation) and $\omega = 0.5$. There is no straining flow in this solution, $A = 0$, and the solution has been started from the multi-mode initial condition with amplitude $\epsilon = 0.03$. The density ratio is $D = 1.05$ and the Froude number is $F = 2$.

$A = 0$, but rotation is present with angular speed parameter $\omega = 0.5$. Density profiles are shown at the two times $t = 3$ and $t = 4$, and only the portion of the solution in the region $-3 < x < 3$, $-3 < y < 3$ is displayed for ease of viewing. At early times, the outflow remains almost spherical, although by time $t = 3$ it is evident that a small waistband structure has begun to form in the profile, as a result of the rotation. After this time, an outflow from each pole develops rather rapidly, so that by time $t = 4$, these structures are quite well developed.

For solutions generated using the multi-mode initial condition in equations (5.1), (5.2), it is observed that qualitatively similar results are indeed obtained as for the monochromatic initial conditions discussed above, namely, that without straining or spin a one-sided outflow is generally produced. This may be converted into a bi-polar flow when rotation or strain are introduced. This is illustrated in Figure 12, for the parameter values used in Figure 11. In this diagram, the picture on the left is for the case of no rotation, $\omega = 0$ and it shows that, once again, an essentially one-sided outflow is produced, similar to that depicted in Figure 7. The density ratio in this diagram is

$D = 1.05$ and the interfaces have been created using the $\bar{\rho} = 0.02$ contour. The remnant of the original sphere is still visible in the diagram for $\omega = 0$, but there is an elongated jet at the top of the diagram, and a much smaller overturning region at the bottom. This is in accordance with the predictions of the linearized theory of Section 2 which indicates that the one-sided mode is the most unstable and so will dominate. When rotation is introduced, however, with angular speed $\omega = 0.5$ in the picture on the right, a strong waistband structure develops, and there is now outflow of roughly similar intensity from each pole. This is closely similar to the situation obtained by starting the flows from a just a single mode, as previously.

# 6 Discussion and Conclusion

This paper has studied outflow of a light fluid from a point source, into a surrounding heavier ambient fluid. The two fluids are separated by an interface which is initially spherical, but a small perturbation is made to the radial velocity component, and this then evolves in time. A linearized theory has been given for the case in which each fluid is incompressible and inviscid, and the interface separating them is infinitessimally thin. The predictions of this theory are then compared with a numerical solution of the viscous Boussinesq equations modelling essentially the same situation. In this approach, the interface is, however, a narrow region of continuous but rapid density change; in addition, the fluid is assumed to be weakly compressible, and the small perturbations to the background density are convected and diffused throughout the flow. Provision has been made for background straining motion of the fluid, and also for solid-body rotation within the inner expanding bubble of lighter fluid ejected from the point source. The numerical solution is achieved using the somewhat novel spectral method advanced by Forbes (2011b), since it has the capacity to treat the point source exactly, even in viscous flow. Furthermore, the spectral method allows the Poisson equation (4.7) to be solved immediately and exactly (see equation 4.16), whereas this can be a difficult task in other solution methods.

In the recent work of Forbes (2011b), the outflow from a point source was studied, and it was found that an inviscid linearized theory predicted that the first spherical Fourier mode is always unstable, and in fact is the fastest growing component. This would mean that an arbitrary initial disturbance, consisting of a mix of all the Fourier modes, would eventually be dominated by the first mode alone. This would result in a one-sided jet emanating from one of the poles of the sphere. This is a surprising conclusion, but it could, in fact, have been derived from an equation given earlier by Plesset

(1954) and Mikaelian (2005). Forbes (2011b) carried out a numerical solution to the non-linear inviscid equations, but that solution was stopped by the formation of a curvature singularity at the interface at critical times that were too early to allow an inviscid one-sided jet to form. However, Forbes' numerical solution of the corresponding viscous Boussinesq model did indeed verify that one-sided jets were produced. This appears to be confirmed by the numerical work of Lovelace et al. (2010).

The main aim of the present paper, therefore, is to determine conditions under which additional flow features might replace this one-sided jet with a bipolar outflow, consisting of an outflow jet emanating from each of the two poles of the sphere. The original motivation for this study came from the astrophysical context, in which bipolar outflows are often observed (see Stahler and Palla 2004), instead of the one-sided flows obtained by Forbes (2011b). Of course, there are many possible explanations for this fact, including the presence of strong magnetic fields, compressibility, shocks and even relativistic effects, all of which are ignored here. Thus, while the original motivation is astrophysical, it remains the case that the present investigation is of interest in its own right, as a study in fundamental fluid mechanics.

Nevertheless, there is now growing evidence that one-sided outflows do genuinely occur in astrophysics. They are predicted by the numerical work of Lovelace et al (2010), and very recently they have also been measured directly by Gómez et al. (2013), in radio observations of the Herbig-Haro object HH 111. The image presented in their figure 1 is taken from the 2007 epoch of that astrophysical source, and it bears a remarkable morphological similarity to the one-sided outflows presented here. Their figure 3 highlights the evolution of this object over the period 1992 – 2007.

It is possible to estimate a likely Froude number for this object HH 111, since it has been the subject of considerable study. Reipurth et al. (1999) indicate that mean outflow speeds are of the order of 150 km/sec, from a source with about 25 Solar luminosities; since this scales as the fourth power of mass, this corresponds to $\sqrt{5}$ Solar masses. If the source radius is comparable to that of the Earth, then $a \approx 6.37 \times 10^6$ metres (see Resnick and Halliday 1966), so that the Froude number in (2.2) is about $F \approx 0.275$. In view of the assumed outflow speed, this is likely to be an upper bound, but in any event, such a small value for the Froude number places this object in a parameter region where moderate values of strain and rotation would be insufficient to prevent the formation of a one-sided jet, as is indeed the case.

A sample computation for $F = 0.275$ is presented in Figure 13. Here, a moderate straining rate $A = 0.05$ and rotation speed $\omega = 0.2$ have been chosen. The solution was started from a perturbation of amplitude $\epsilon = 0.01$ to the first Fourier mode $n = 1$, as in equation (4.24). A one-sided jet begins

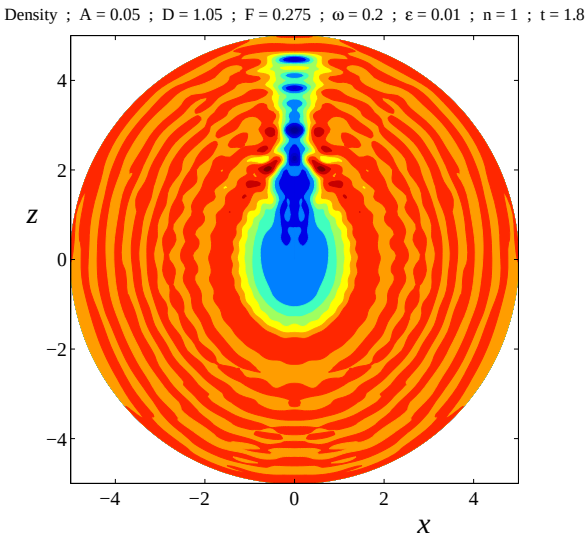


Figure 13: Density contours at time $t = 1.8$, for an outflow at Froude number $F = 0.275$. The straining parameter is $A = 0.05$, with density ratio $D = 1.05$ and angular speed parameter $\omega = 0.2$. The solution was started at the first Fourier mode, $n = 1$ with initial amplitude $\epsilon = 0.01$. The scale on both axes is the same.

to form in the interface at about $t = 1$ and is well established by time $t = 1.8$, as is evident in Figure 13.

Thus the theoretical results of the present paper show that, for small amplitude deformations in the infinite Froude number limit, a straining flow alone is sufficient to convert the one-sided outflow found by Forbes (2011b) into a genuinely bipolar flow. This is discussed in Section 2.1. Similarly, rotation about the $z$-axis also results in a bipolar flow as $F \to \infty$, although with reduced outflow from the poles and a correspondingly enlarged waistband, as discussed in Section 3.1. However, the result is considerably less clear in the case of finite Froude number, although in most instances it appears no longer to be true; the analytical solutions in Sections 2 and 3 appear to suggest that the mode-one solutions are again the most unstable, so that one-sided outflows are therefore most likely to be encountered.

Viscous Boussinesq theory confirms the predictions of the linearized theory of Section 2 for finite Froude number $F$, when the imposed strain rate is sufficiently small. In these viscous results, the diffusion constant in equation (4.10) was set simply to $\sigma = 10^{-4}$ and the Reynolds number in equation (4.8) was taken to be $R_e = 250$, as in Forbes (2011b), although the solutions are not qualitatively affected by this choice. As the strain rate parameter $A$ is made larger, however, linearized theory eventually ceases to be valid so that, for sufficiently large $A$, the non-linear results show clearly that the imposed strain field is again sufficient to produce genuinely bipolar outflows. These are nevertheless complex structures, and the two outflow jets are not exactly symmetric about the centre-plane. It is, perhaps, not unreasonable to expect that a strong strain field in a viscous fluid will create an essentially bipolar outflow, since the straining flow itself consists of the second spherical Fourier mode, which is bipolar. It might be possible in future work to investigate the relationship between straining fields and the morphologies they generate using a weakly non-linear theory, although this has so far eluded the present investigation.

The viscous Boussinesq solution presented here has also shown that sufficiently strong rotation in the inner lighter fluid can also be responsible for producing a type of bipolar outflow, rather than the purely one-sided flows of Forbes (2011b). This is in accordance with the weakly non-linear solution of Section 3 for inviscid fluids. However, these non-linear flows are rather complex; the two outflow jets are again not entirely symmetric, and there is evidently also a transfer of energy out of the azimuthal rotation mode and into the azimuthal component $Z$ of vorticity, that causes rotation in a plane normal to the azimuthal direction. At this point, it is reasonable to ask whether these axi-symmetric structures would be stable to small perturbations in the azimuthal coordinate $\theta$. This would then generate a fully three-dimensional

flow, and has been ignored here. Nevertheless, much interesting stability analysis remains to be done in that case. The corresponding numerical solutions could in principle be obtained by an extension of the spectral method developed here, although that would require formidable computational resources. A very recent study by Romanova et al. (2013) has considered fully three-dimensional magnetohydrodynamic waves in the accretion disks of rotating stars, and a curved one-armed wave was shown. Similar results may be possible in the present problem also, but await future study.

# 7 Acknowledgements:

This work has been carried out in association with ARC (Australian Research Council) discovery grant DP140100094. Comments by three anonymous Referees are gratefully acknowledged.

# 8 Appendix A - Full Solution of the Linearized Equations

In this Appendix, a complete closed-form solution is presented to the linearized equations (2.16), (2.17) in Section 2.

Since the governing equations are linear, the Fourier-Legendre modes decouple, and so may be considered separately, as before. Rather than using time $t$ as the independent variable, the zeroth-order radius function $R_0(t) = \left[1 + (3t)/(4\pi)\right]^{1/3}$ in equation (2.8) is employed instead. This change of variables converts equation (2.16) into

$$R_0^2 \frac{d^2 R_{n1}}{dR_0^2} + R_0 \frac{dR_{n1}}{dR_0}$$
$$- R_{n1}\left[\frac{2[(n+2)(n+1) - Dn(n-1)]}{(Dn+n+1)} + (D-1)\frac{(4\pi)^2}{F^2}\frac{n(n+1)}{(Dn+n+1)}R_0^3\right] = 0$$
if $n \neq 2$.

This equation is next subjected to the further change of independent variable

$$\xi = \lambda_n R_0^{3/2} \quad \text{with } \lambda_n = \frac{2}{3}\frac{(4\pi)}{F}\sqrt{(D-1)\frac{n(n+1)}{(Dn+n+1)}}.$$

As a result, it is reduced to the form

$$\xi^2 \frac{d^2 R_{n1}}{d\xi^2} + \xi \frac{dR_{n1}}{d\xi} - \left(\xi^2 + \nu_n^2\right) R_{n1} = 0, \tag{8.1}$$

in which the auxiliary constant $\nu_n$ is defined to be

$$\nu_n = \sqrt{\frac{8}{9}\left[\frac{(n+2)(n+1) - Dn(n-1)}{(Dn+n+1)}\right]}. \tag{8.2}$$

Equation (8.1) is a modified Bessel equation (see Abramowitz and Stegun (1972), page 374). It then follows that the closed-form solution to equation (2.16) is

$$R_{n1}(R_0) = C_1 I_{\nu_n}\left(\lambda_n R_0^{3/2}\right) + C_2 K_{\nu_n}\left(\lambda_n R_0^{3/2}\right), \tag{8.3}$$

in which $I_\nu$ and $K_\nu$ are modified Bessel functions of the first and second kinds, respectively, and the two constants $C_1$ and $C_2$ are arbitrary. For $D > 1$, which is the case of most interest here, the first-kind modified Bessel function grows exponentially with radius function $R_0$ , but only for certain of the lowest modes, for which the order $\nu_n$ in equation (8.2) is real. Therefore only a select few of the lowest-order modes are unstable.

The same changes of variable are also made to the second-mode equation (2.17). After some algebra, it reduces to the inhomogeneous modified Bessel equation

$$\xi^2 \frac{d^2 R_{21}}{d\xi^2} + \xi \frac{dR_{21}}{d\xi} - \left(\xi^2 + \nu_2^2\right) R_{21} = A_1 \Gamma_2 \xi^{8/3}, \tag{8.4}$$

in which the constant $\nu_2$ is obtained from (8.2). The parameter $A_1$ is again the linearized straining amplitude, and

$$\Gamma_2 = \frac{80D}{9(2D+3)} \frac{(4\pi)}{\lambda_2^{8/3}}$$

has been defined for convenience. The inhomogeneous equation (8.4) can be solved using a variation of parameters approach (see Kreyszig 2011) and the Wronskian

$$I_\nu(\xi) K'_\nu(\xi) - K_\nu(\xi) I'_\nu(\xi) = \frac{1}{\xi}$$

The general solution may therefore be written in the form

$$\begin{aligned} R_{21}(\xi) &= C_1 I_{\nu_2}(\xi) + C_2 K_{\nu_2}(\xi) \\ &+ A_1 \Gamma_2 \int_{\lambda_2}^{\xi} u^{11/3} \left[I_{\nu_2}(\xi) K_{\nu_2}(u) - K_{\nu_2}(\xi) I_{\nu_2}(u)\right] du. \end{aligned} \tag{8.5}$$

It is very difficult to compare the solution (8.5) for the second mode $n = 2$ with the result (8.3) for $n \neq 2$ to determine which mode has the fastest growth rate. So it is evidently not possible for general $F$ and $D$ to determine whether straining forces the one-sided jet to become bipolar, at least

in linearized theory. However, the additional integral term in (8.5) due to straining appears to grow algebraically, whereas the lowest-order mode $R_{11}$ in (8.3) can grow exponentially. Thus it appears to be the case that, in general, a one-sided outflow is predicted by linearized theory.

# 9 Appendix B - ODEs for Viscous Fourier Coefficients

This Appendix gives the complete set of ordinary differential equations satisfied by the Fourier coefficients in the Boussinesq viscous model outlined in section 4.

The vorticity equation (4.8) is subjected to Fourier analysis, as described in section 4. This leads to the system of $MN$ ordinary differential equations

$$\begin{aligned}
\frac{dB_{k\ell}}{dt} &= -\frac{1}{F^2\alpha_{\ell,k}^2}C_{k\ell}(t) - \frac{1}{R_e}\alpha_{\ell,k}^2 B_{k\ell}(t) \\
&+ \frac{(2\ell+1)}{\ell(\ell+1)\big[\alpha_{\ell,k}\beta J_{\ell+3/2}\big(\alpha_{\ell,k}\beta\big)\big]^2}\int_0^\beta\int_0^\pi\Big[\sqrt{r}Z\big(u\sin\phi + w\cos\phi\big) \\
&\qquad -\sqrt{r}\big(ru\frac{\partial Z}{\partial r} + w\frac{\partial Z}{\partial\phi}\big)\sin\phi - \frac{2v}{\sqrt{r}}\big(\frac{\partial v}{\partial\phi}\sin\phi - r\cos\phi\frac{\partial v}{\partial r}\big)\Big] \\
&\qquad \times J_{\ell+1/2}\big(\alpha_{\ell,k}r\big)P_\ell'(\cos\phi)\sin\phi\,d\phi\,dr \\
&\quad k = 1,2,\ldots,M, \quad \ell = 1,2,\ldots,N.
\end{aligned}$$

When the azimuthal component (4.8) of the Boussinesq Navier-Stokes equations is similarly analyzed as described in the text, it yields

$$\begin{aligned}
\frac{dV_{k\ell}}{dt} &= -\frac{1}{R_e}\alpha_{\ell,k}^2\big(\delta_{1,\ell}V_{k0}^S + V_{k\ell}(t)\big) \\
&- \frac{(2\ell+1)}{\ell(\ell+1)\big[\beta J_{\ell+3/2}\big(\alpha_{\ell,k}\beta\big)\big]^2}\int_0^\beta\int_0^\pi \\
&\qquad \Big[\sqrt{r}v\big(u\sin\phi + w\cos\phi\big) + \sqrt{r}\big(ru\frac{\partial v}{\partial r} + w\frac{\partial v}{\partial\phi}\big)\sin\phi\Big] \\
&\qquad \times J_{\ell+1/2}\big(\alpha_{\ell,k}r\big)P_\ell'(\cos\phi)\sin\phi\,d\phi\,dr \\
&\quad k = 1,2,\ldots,M, \quad \ell = 1,2,\ldots,N.
\end{aligned}$$

The Kronecker delta symbol $\delta_{1,\ell}$ in this equation takes the value 1 when $\ell = 1$ and 0 otherwise.

The density equation (4.10) is also decomposed into its Fourier modes, and gives the further system of differential equations

$$\begin{aligned}
\frac{dC_{k0}}{dt} &= -\frac{3}{\beta^3}\int_0^\beta\int_0^\pi\left(u\frac{\partial\bar\rho}{\partial r}+\frac{w}{r}\frac{\partial\bar\rho}{\partial\phi}\right)r^2\sin\left(\frac{k\pi r^3}{\beta^3}\right)\sin\phi\,d\phi\,dr \\
&+ \frac{72\sigma(D-1)}{\beta^3}\int_0^\beta\left(\frac{r}{\beta}\right)^3\sin\left(\frac{k\pi r^3}{\beta^3}\right)dr \\
&+ \frac{6\sigma}{\beta^3}\sum_{m=1}^M C_{m0}(t)\Bigg[12m\pi\int_0^\beta\left(\frac{r}{\beta}\right)^3\cos\left(\frac{m\pi r^3}{\beta^3}\right)\sin\left(\frac{k\pi r^3}{\beta^3}\right)dr \\
&\qquad -9m^2\pi^2\int_0^\beta\left(\frac{r}{\beta}\right)^6\sin\left(\frac{m\pi r^3}{\beta^3}\right)\sin\left(\frac{k\pi r^3}{\beta^3}\right)dr\Bigg], \\
&\qquad k=1,2,\ldots,M
\end{aligned}$$

for the zeroth-order coefficients $C_{k0}(t)$. The higher-order coefficients $C_{k\ell}(t)$ for the modes of order $\ell$ in the variable $\phi$ are then determined from

$$\begin{aligned}
\frac{dC_{k\ell}}{dt} &= -\sigma\big(\alpha_{\ell,k}\big)^2C_{k\ell}(t) \\
&- \frac{(2\ell+1)}{\beta^2J^2_{\ell+3/2}\big(\alpha_{\ell,k}\beta\big)}\int_0^\beta\int_0^\pi\left(u\frac{\partial\bar\rho}{\partial r}+\frac{w}{r}\frac{\partial\bar\rho}{\partial\phi}\right)\frac{J_{\ell+1/2}\big(\alpha_{\ell,k}r\big)}{r^{3/2}}P_\ell(\cos\phi)\sin\phi\,d\phi\,dr \\
&+ \frac{2\sigma}{\beta^2J^2_{\ell+3/2}\big(\alpha_{\ell,k}\beta\big)}\sum_{m=1}^M C_{m\ell}(t)\Bigg[6\alpha_{\ell,m}\int_0^\beta J'_{\ell+1/2}\big(\alpha_{\ell,m}r\big)J_{\ell+1/2}\big(\alpha_{\ell,k}r\big)\,dr \\
&\qquad +9\int_0^\beta r^{-1}J_{\ell+1/2}\big(\alpha_{\ell,m}r\big)J_{\ell+1/2}\big(\alpha_{\ell,k}r\big)\,dr\Bigg], \\
&\qquad k=1,2,\ldots,M,\quad \ell=1,2,\ldots,N.
\end{aligned}$$

# 10 Bibliography


M. Abramowitz and I.A. Stegun (editors) (1972). *Handbook of Mathematical Functions*. Dover, New York.

S. Anathpindika (2009). Supersonic cloud collision. I. *Astron. and Astrophys.*, **504**, 437–450. `http://dx.doi.org/10.1051/0004-6361/200911748`

G. Baker, R.E. Caflisch and M. Siegel (1993). Singularity formation during Rayleigh-Taylor instability. *J. Fluid Mech.*, **252**, 51–78. `http://dx.doi.org/10.1017/S0022112093003660`

G.R. Baker and L.D. Pham (2006). A comparison of blob methods for vortex sheet roll-up. *J. Fluid Mech.*, **547**, 297–316. http://dx.doi.org/10.1017/S0022112005007305

G.K. Batchelor (1967). *An Introduction to Fluid Dynamics*. Cambridge University Press, Cambridge.

J. Braine, U. Lisenfeld, P.-A. Duc, E. Brinks, V. Charmandaris and S. Leon (2004). Colliding molecular clouds in head-on galaxy collisions. *Astron. and Astrophys.*, **418**, 419–428. http://dx.doi.org/10.1051/0004-6361:20035732

K. Chambers and L.K. Forbes (2012). The cylindrical magnetic Rayleigh-Taylor instability for viscous fluids. *Phys. Plasmas*, **19**, article 102111, 13 pages. http://dx.doi.org/10.1063/1.4759453

S. Chandrasekhar (1961). *Hydrodynamic and Hydromagnetic Stability*. Dover Inc., New York.

S.J. Cowley, G.R. Baker and S. Tanveer (1999). On the formation of Moore curvature singularities in vortex sheets. *J. Fluid Mech.*, **378**, 233–267. http://dx.doi.org/10.1017/S0022112098003334

A.Q. Cui and R.L. Street (2004). Large-eddy simulation of coastal upwelling flow. *Environ. Fluid Mech.*, **4**, 197–223. http://dx.doi.org/10.1023/B:EFMC.0000016610.05554.0f

R. Dgani and N. Soker (1998). Instabilities in moving planetary nebulae. *Astrophys. J.*, **495**, 337–345. http://dx.doi.org/10.1086/305257

P.G. Drazin and W.H. Reid (2004). *Hydrodynamic Stability*, Second Edition. Cambridge University Press, Cambridge.

R. Epstein (2004). On the Bell-Plesset effects: The effects of uniform compression and geometrical convergence on the classical Rayleigh-Taylor instability. *Phys. Plasmas*, **11**, 5114–5124. http://dx.doi.org/10.1063/1.1790496

D.E. Farrow and G.C. Hocking (2006). A numerical model for withdrawal from a two-layer fluid. *J. Fluid Mech.*, **549**, 141–157. http://dx.doi.org/10.1017/S0022112005007561

L.K. Forbes (2009). The Rayleigh-Taylor instability for inviscid and viscous fluids. *J. Engin. Math.*, **65**, 273–290. http://dx.doi.org/10.1007/s10665-009-9288-9

L.K. Forbes (2011a). A cylindrical Rayleigh-Taylor instability: radial outflow from pipes or stars. *J. Engin. Math.*, **70**, 205–224. http://dx.doi.org/10.1007/s10665-010-9374-z

L.K. Forbes (2011b). Rayleigh-Taylor instabilities in axi-symmetric outflow from a point source. *ANZIAM J.*, **53**, 87–121. http://dx.doi.org/10.1017/S1446181112000090

L.K. Forbes and M.A. Brideson (2013). Exact solutions for interfacial outflows with straining. *ANZIAM J.*, to appear.

L. Gómez, L.F. Rodríguez and L. Loinard (2013). A one-sided knot ejection at the core of the HH 111 outflow. *Revista Mexicana Astron. Astro.*, **49**, 79–85.

I.S. Gradshteyn and I.M. Ryzhik (2000). *Tables of Integrals, Series and Products, sixth edition.* Academic Press, San Diego.

M. Huarte-Espinosa, A. Frank, B. Balick, E.G. Blackman, O. de Marco, J.H. Kastner and R. Sahai (2012). From bipolar to elliptical: simulating the morphological evolution of planetary nebulae. *Mon. Not. R. Astron. Soc.*, **424**, 2055–2068. http://dx.doi.org/10.1111/j.1365-2966.2012.21348.x

N.A. Inogamov (1999). The role of Rayleigh-Taylor and Richtmyer-Meshkov instabilities in astrophysics: an introduction. *Astrophys. Space Phys.*, **10**, 1–335.

T. Inoue and Y. Fukui (2013). Formation of massive molecular cloud cores by cloud-cloud collision. *Astrophys. J. Letters*, **774** article L31, 5 pages. http://dx.doi.org/10.1088/2041-8205/774/2/L31

R.I. Klein and D.T. Woods (1998). Bending mode instabilities and fragmentation in interstellar cloud collisions: a mechanism for complex structure. *Astrophys. J.*, **497**, 777–799. http://dx.doi.org/10.1086/305488

R. Krasny (1986). Desingularization of periodic vortex sheet roll-up. *J. Comput. Phys.*, **65**, 292–313. http://dx.doi.org/10.1016/0021-9991(86)90210-X

E. Kreyszig (2011). *Advanced Engineering Mathematics, tenth edition.* Wiley, New York.

R.V.E. Lovelace, M.M. Romanova, G.V. Ustyugova and A.V. Koldoba (2010). One-sided outflows/jets from rotating stars with complex magnetic fields. *Mon. Not. R. Astron. Soc.*, **408**, 2083–2091. http://dx.doi.org/10.1111/j.1365-2966.2010.17284.x

M.-M. M. Low and R.S. Klessen (2004). Control of star formation by supersonic turbulence. *Rev. Modern Phys.*, **76**, 125–194. http://dx.doi.org/10.1103/RevModPhys.76.125

M.-M. M. Low and R. McCray (1988). Superbubbles in disk galaxies. *Astrophys. J.*, **324**, 776–785. http://dx.doi.org/10.1086/165936

C. Matsuoka and K. Nishihara (2006). Analytical and numerical study on a vortex sheet in incompressible Richtmyer-Meshkov instability in cylindrical geometry. *Phys. Rev. E*, **74**, article 066303, 12 pages. http://dx.doi.org/10.1103/PhysRevE.74.066303

N.M. McClure-Griffiths, J.M. Dickey, B.M. Gaensler and A.J. Green (2003). Loops, drips, and walls in the galactic chimney GSH 277 + 00 + 36. *Astrophys. J.*, **594**, 833–843. http://dx.doi.org/10.1086/377152

K.O. Mikaelian (2005). Rayleigh-Taylor and Richtmyer-Meshkov instabilities and mixing in stratified cylindrical shells. *Phys. Fluids*, **17**, article 094105, 13 pages. http://dx.doi.org/10.1063/1.2046712

D.W. Moore (1979). The spontaneous appearance of a singularity in the shape of an evolving vortex sheet. *Proc. Roy. Soc. London A*, **365**, 105–119. http://dx.doi.org/10.1098/rspa.1979.0009

J. Nordhaus, T.D. Brandt, A. Burrows and A. Almgren (2012). The hydrodynamic origin of neutron star kicks. *Mon. Not. R. Astron. Soc.*, **423**, 1805–1812. http://dx.doi.org/10.1111/j.1365-2966.2012.21002.x

M.S. Plesset (1954). On the Stability of Fluid Flows with Spherical Symmetry. *L. Appl. Phys.*, **25**, 96–98. http://dx.doi.org/10.1063/1.1721529

Lord Rayleigh (1883). Investigation of the character of the equilibrium of an incompressible heavy fluid of variable density. *Proc. London Math. Soc.*, **14**, 170–177.

B. Reipurth and J. Bally (2001). Herbig-Haro flows: probes of early stellar evolution. *Ann. Rev. Astron. Astrophys.*, **39**, 403–455. http://dx.doi.org/10.1146/annurev.astro.39.1.403

B. Reipurth, K.C. Yu, L.F. Rodríguez, S. Heathcote and J. Bally (1999). Multiplicity of the HH 111 jet source: *Hubble Space Telescope* NICMOS images and VLA maps. *Astron. Astrophys.*, **352**, L83–L86.

R. Resnick and D. Halliday (1966). *Physics*. Wiley International Edition, Toppan Printing Co., Japan.

M.M. Romanova, G.V. Ustyugova, A.V. Koldoba and R.V.E. Lovelace (2013). Warps, bending and density waves excited by rotating magnetized stars: results of global 3D MHD simulations. *Mon. Not. R. Astron. Soc.*, **430**, 699–724. http://dx.doi.org/10.1093/mnras/sts670

R.W. Schmitt (1995). The salt finger experiments of Jevons (1857) and Rayleigh (1880). *J. Phys. Oceanography*, **25**, 8–17. http://dx.doi.org/10.1175/1520-0485(1995)025<0008:TSFEOJ>2.0.CO;2

K. Shariff (2009). Fluid mechanics in disks around young stars. *Annu. Rev. Fluid Mech.*, **41**, 283–315. http://dx.doi.org/10.1146/annurev.fluid.010908.165144

D.H. Sharp (1984). An overview of Rayleigh-Taylor instability. *Physica D*, **12**, 3–18. http://dx.doi.org/10.1016/0167-2789(84)90510-4

S.W. Stahler and F. Palla (2004). *The Formation of Stars*. Wiley - VCH, Berlin.

Sir G.I. Taylor (1950). The instability of liquid surfaces when accelerated in a direction perpendicular to their planes, I. *Proc. Roy. Soc. London Ser. A*, **201**, 192–196.

G. Tryggvason, W.J.A. Dahm and K. Sbeih (1991). Fine structure of vortex sheet rollup by viscous and inviscid simulation. *J. Fluids Engineering*, **113**, 31–36. http://dx.doi.org/10.1115/1.2926492

G. von Winckel (2004). *lgwt.m* . at: MATLAB file exchange website. http://www.mathworks.com/matlabcentral/fileexchange/loadFile.do?objectId=4540&objectType=file

W.-H. Ye, L.-F. Wang and X.-T. He (2010). Jet-like long spike in nonlinear evolution of ablative Rayleigh-Taylor instability. *Chin. Phys. Lett.*, **12**, article 125203, 4 pages. http://dx.doi.org/10.1088/0256-307X/27/12/125203

H. Zinnecker and H.W. Yorke (2007). Toward understanding massive star formation. *Ann. Rev. Astron. Astrophys.*, **45**, 481–563. http://dx.doi.org/10.1146/annurev.astro.44.051905.092549